Pseudo-unsteady Two-dimensional Viscous-Inviscid Interaction Method for Steady Transonic Flows

Paul Dechamps[†*], Amaury Bilocq[†], Adrien Crovato[‡], Grigorios Dimitriadis[§], and Vincent E. Terrapon[§]
University of Liège, 4000 Liège, Belgium

Driven by increasingly stringent efficiency requirements, aerodynamic optimization is nowadays integrated early in the design process of new aircraft. Quick evaluation of the performance of one design configuration can be obtained by using methods based on viscous-inviscid interaction. These approaches usually come at a lower computational cost than RANS computations, and predict more accurate values for the aerodynamic loads and improve shock modeling in transonic conditions compared to purely inviscid techniques. This study presents a novel two-dimensional pseudo-time-dependent formulation of the viscous compressible boundary layer equations in the context of the quasi-simultaneous coupling strategy for steady viscous-inviscid calculations of compressible transonic flows in external aerodynamics. The proposed methodology is first evaluated on subsonic attached and mildly separated flows around a symmetrical airfoil at a high angle of attack. Predictions in transonic configurations are then shown on symmetrical and supercritical airfoils and are compared to RANS solutions and experimental measurements. Good agreement with reference results is observed for flows with limited separation regions and for transonic flows.

I. Nomenclature

ξ, η	=	tangential and normal coordinates in the local frame of reference
u	=	velocity component in the ξ-direction
v	=	velocity component in the η-direction
p	=	pressure
M	=	Mach number
ρ	=	density
μ	=	fluid dynamic viscosity
ν	=	fluid kinematic viscosity

[*]paul.dechamps@uliege.be
[†]PhD. candidate, Aerospace and Mechanical engineering departement
[‡]Postdoctoral researcher, Aerospace and Mechanical engineering departement
[§]Professor, Aerospace and Mechanical engineering departement

$\cdot_\infty$ = quantity evaluated in the freestream

$\cdot_e$ = quantity evaluated at the edge of the boundary layer

U_∞ = freestream velocity

δ^* = displacement thickness, $\int_0^\infty [1 - (\rho u/\rho_e u_e)] \mathrm{d}\eta$

δ^{**} = density thickness, $\int_0^\infty (u/u_e)[1 - (\rho/\rho_e)] \mathrm{d}\eta$

θ = momentum thickness, $\int_0^\infty \rho u/\rho_e u_e [1 - (u/u_e)] \mathrm{d}\eta$

θ^* = kinetic energy thickness, $\int_0^\infty \rho u/\rho_e u_e [1 - (u^2/u_e^2)] \mathrm{d}\eta$

H = shape factor of the boundary layer, δ^*/θ

H^* = kinetic energy shape parameter, θ^*/θ

H^{**} = density shape parameter, δ^{**}/θ

τ_S = shear stress

$c_{d,l}$ = local dissipation coefficient, $(1/\rho_e u_e^3) \int_0^\infty \tau_S (\partial u/\partial \eta) \mathrm{d}\eta$

$c_{f,l}$ = local skin-friction coefficient, $2\tau_{S,\mathrm{wall}}/\rho_e u_e^2$

Re_θ = local momentum thickness Reynolds number, $\rho_e u_e \theta/\mu_e$

h = height of the first cell at the wall

$\tilde{c}$ = cell coefficient, $4U_\infty/(\pi h)$

c = airfoil chord length

α = angle of attack

c_p = pressure coefficient, $2(p - p_\infty)/\rho_\infty U_\infty^2$

c_l = lift coefficient

c_d = drag coefficient

c_f = global skin-friction coefficient, $2\tau_{S,\mathrm{wall}}/\rho_\infty U_\infty^2$

II. Introduction

Nowadays, the aerodynamic properties of aircraft are usually obtained by calculating solutions of the Reynolds-Averaged Navier-Stokes (RANS) equations, which usually come at the cost of expensive computations that are impractical in early design stages. An adequate aerodynamic insight can be obtained by making use of lower fidelity methods, such as *viscous-inviscid interaction* (VII) methods, whereby a viscous correction based on the integral boundary layer equations is applied to an inviscid flow through a coupling methodology. These approaches can be used routinely in optimization processes and are suited to assess aircraft model variations when a large number of design variables is considered. However, they can suffer from numerical instabilities when separations, transitions or shocks are present in the flow. This work introduces a novel coupled boundary layer methodology for laminar and turbulent

compressible steady flows around wing profiles that can be used flexibly with existing inviscid solvers. The primary objective is to develop a tool for studying high Reynolds number steady transonic flows at the initial stages of aircraft design. The proposed method has been implemented in a free and open-source solver named BLASTER (Boundary Layer Adjoint Solver for Transonic External High Reynolds Number Flow).*

In a VII methodology, any inviscid flow solver can be utilized. The Euler equations have yielded good results in the literature [1–3], but solutions of these equations still come at a computational cost that might be too high for preliminary aircraft design applications. Linearized potential methods can be used to reduce the computational cost [4–6], but this leads to poor predictions of the non-linear effects occurring in the transonic regime, which makes these approaches unsuitable for the present application. Transonic flow solutions with embedded weak shock waves can be obtained at a low computational cost by considering the non-linear compressible potential flow equation [7, 8].

The viscous calculation is typically carried out by solving the integral boundary layer equations (IBL) [1, 3, 5, 7]. The steady IBL set of equations for a compressible flow, presented by Giles and Drela [9], allows the modeling of attached and mildly separated flows. However, obtaining the numerical solution becomes challenging in the presence of strong pressure gradients, such as those occurring near suction peaks, in separation regions, close to the trailing edge, or at the impingement of shock waves. These conditions often lead to difficulties in converging the solution toward a steady state, for example when the inviscid solution demonstrates oscillations. Recent studies [5, 6, 10, 11] have shown that the use of unsteady integral boundary layer equations can partially address the numerical difficulties associated with strong adverse pressure gradients. In particular, the unsteady formulation improves numerical robustness and facilitates convergence toward a steady solution in mildly separated flows. In addition to these numerical convergence issues, the steady IBL equations exhibit a fundamental limitation in separated laminar flows: the appearance of the Goldstein singularity [12]. This singular behavior arises when the pressure is directly imposed as a boundary condition in the viscous solver, which becomes incompatible with the boundary-layer equations in regions of flow separation. Although the unsteady terms of the time-dependent IBL mitigate convergence issues, they do not fundamentally remove the Goldstein singularity, which is directly related to the pressure boundary condition. As demonstrated by van Dommelen and Shen [13], the unsteady equations may still fail to produce a physically correct solution for separating flows.

In order to avoid the singular behavior associated with directly imposing pressure, more advanced coupling strategies have been developed. These methods aim to reformulate the coupling such that the viscous solver is not forced by the pressure distribution. The main existing methods are direct, inverse, semi-inverse, fully-simultaneous and quasi-simultaneous coupling. In inverse and semi-inverse methods, this is achieved by prescribing the displacement thickness to the viscous solver rather than the pressure, allowing the inviscid solver to adjust the pressure field accordingly [14–16]. In the inverse method, the boundary layer displacement thickness is given as input to the viscous solver. The viscous solver then computes the pressure, given as input to the inviscid solver. In the semi-inverse method, the displacement

*Free and Open Source implementation: `https://gitlab.uliege.be/am-dept/blaster`, accessed March 2025

thickness is given to both the viscous and inviscid solvers, and both compute the pressure. The interaction is done using a relaxation formula, which combines the pressures given by both solvers to compute the new displacement thickness. However, these two techniques usually lead to a higher computational cost of the coupled algorithm. Fully-simultaneous and quasi-simultaneous coupling strategies extend this idea further. In the fully-simultaneous approach, the inviscid and viscous equations are solved together in a unified system, providing an exact representation of the inviscid flow as a boundary condition for the boundary layer [1, 7]. However, the fully-simultaneous approach cannot be easily used with existing inviscid solvers, as it requires significant modifications of the latter. In contrast, the quasi-simultaneous method relies on an approximate inviscid-flow model while still avoiding the direct prescription of pressure [17–20]. These approaches improve robustness in high-pressure-gradient flows, and prevent the formation of the Goldstein singularity, but at a higher computational cost than the fully-simultaneous technique.

The approach proposed here is based on the quasi-simultaneous coupling strategy in which the IBL equations introduced by Drela and Giles [1] are expressed in a novel pseudo-unsteady form to enhance robustness and stability in numerically challenging cases. More specifically, the algorithm consists in a succession of inviscid and viscous iterations. The inviscid flow is obtained by solving the steady compressible potential equations using the non-linear potential flow solver DART [21]. The viscous boundary layer is computed using a classical space marching approach in which each streamwise location is treated individually. At each location the pseudo-unsteady IBL equations, whose time-dependent terms do not include compressible effects, are solved in time. A dissipative implicit time integration scheme controlled by an adaptive CFL is used in conjunction with a damped-Newton solver to quickly damp the initial transient. In addition, the interaction law proposed by Veldman is modified into a pseudo-time-dependent differential equation that is solved together with the IBL equations. Finally, the location of the laminar-turbulent transition is computed by the e^N method [22, 23], also formulated in a pseudo-unsteady form.

The proposed approach offers an interesting alternative to improve the convergence of the quasi-simultaneous coupling in challenging transonic cases with only a single user-defined parameter, the CFL number. Generally, for two-dimensional problems, the algorithm converges in a one second for subsonic cases and five seconds for transonic flows using accurate grids.

The present document is organized as follows. The mathematical model used in the viscous calculation is presented in Section III. Section IV describes the coupling strategy and how it has been adapted to the proposed model. Details about the numerical method used to solve the boundary layer system of equations and quickly reach steady states are given in Section V. Results obtained with the new method are presented in Section VI and are compared to higher fidelity data. Finally, conclusions and perspectives for future work are given in Section VII.

III. Pseudo-Unsteady Modeling of Boundary Layer Flow

The main novelty of the present work is to use a pseudo-unsteady form of the compressible boundary layer equations to solve for the viscous part of the flow. Because only steady aerodynamic predictions are of interest here, the unsteady boundary layer equations are simplified while keeping the properties of the system that can prevent the numerical difficulties encountered in viscous-inviscid interaction schemes. The following presents the details of the mathematical model used in the present method in order to perform viscous-inviscid calculations.

This study relies on DART, a full-potential finite element-based solver designed for aerodynamic and aeroelastic computations, to calculate the inviscid flow solution [24, 25]. The computation of the flow inside the boundary layer is done by considering a two-dimensional coordinate system attached to the body, (ξ, η) with ξ pointing in the downstream direction and η normal to, and pointing away from, the solid wall surface, as shown in Fig. 1.

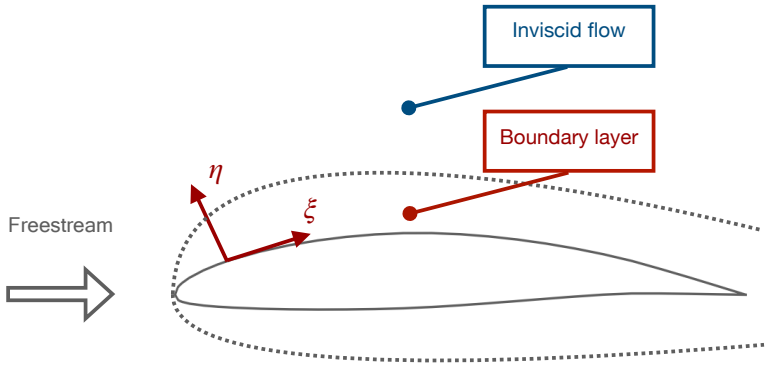

Fig. 1 Representation of the local coordinate system, where (ξ, η) denote tangential and normal surface directions, respectively. The dotted line marks the boundary-layer edge.

The strategy well established in the literature [15, 18, 20, 26–28] is used to derive the IBL equations. The steady compressible equations are presented by Giles and Drela [9],

$$\frac{\partial \theta}{\partial \xi} + (2 + H - M_e^2)\frac{\theta}{u_e}\frac{\partial u_e}{\partial \xi} - \frac{c_{f,l}}{2} = 0 \tag{1}$$

$$\theta \frac{dH^*}{d\xi} + (2H^{**} + H^*(1 - H))\frac{\theta}{u_e}\frac{\partial u_e}{\partial \xi} - 2c_{d,l} + H^*\frac{c_{f,l}}{2} = 0, \tag{2}$$

where θ is the momentum thickness and H the shape factor of the boundary layer. The local velocity, u_e, and Mach number, M_e, are defined at the boundary layer's outer edge. The local friction coefficient $c_{f,l}$ is defined at the wall, and $c_{d,l}$ represents the dissipation coefficient due to viscous effects. Finally, H^* and H^{**} are the kinetic energy and density shape parameters. The unsteady incompressible boundary layer system is given by Van Es [10] from White [29],

$$\frac{1}{u_e^2}\left(u_e H\frac{\partial \theta}{\partial t} + u_e\theta\frac{\partial H}{\partial t} + \theta H\frac{\partial u_e}{\partial t}\right) = -\frac{\partial \theta}{\partial \xi} - \frac{\theta}{u_e}(2 + H)\frac{\partial u_e}{\partial \xi} + \frac{c_{f,l}}{2} \tag{3}$$

$$
\begin{aligned}
&2\frac{1}{H^* u_e^2}\frac{\partial u_e}{\partial t} - \frac{H}{u_e \theta}\frac{\partial \theta}{\partial t} - \frac{1}{u_e}\frac{\partial H}{\partial t} - \frac{H}{u_e^2}\frac{\partial u_e}{\partial t} + \frac{1}{u_e H^* \theta}\frac{\partial \theta}{\partial t} + \frac{1}{u_e H^* \theta}\left(H\frac{\partial \theta}{\partial t} + \theta\frac{\partial H}{\partial t}\right) \\
&= -(1-H)\frac{1}{u_e}\frac{\partial u_e}{\partial \xi} - \frac{1}{H^*}\frac{\partial H^*}{\partial \xi} + \frac{c_{d,l}}{H^* \theta} - \frac{1}{2}\frac{c_{f,l}}{\theta}.
\end{aligned} \tag{4}
$$

In order to obtain the pseudo-unsteady system, compressible effects are only taken into account for the steady terms of the equations. Injecting the unsteady terms of Eqs. (3) and (4) into Eqs. (1) and (2) yields the pseudo-unsteady boundary layer equations,

$$
\frac{H}{u_e}\frac{\partial \theta}{\partial \tau} + \frac{\theta}{u_e}\frac{\partial H}{\partial \tau} + \frac{\theta H}{u_e^2}\frac{\partial u_e}{\partial \tau} = -\frac{\partial \theta}{\partial \xi} - (2 + H - M_e^2)\frac{\theta}{u_e}\frac{\partial u_e}{\partial \xi} + \frac{c_{f,l}}{2}, \tag{5}
$$

$$
\frac{1 + H(1-H^*)}{u_e}\frac{\partial \theta}{\partial \tau} + \frac{\theta(1-H^*)}{u_e}\frac{\partial H}{\partial \tau} + \frac{\theta(2 - H^* H)}{u_e^2}\frac{\partial u_e}{\partial \tau} = -\theta\frac{dH^*}{d\xi} - (2H^{**} + H^*(1-H))\frac{\theta}{u_e}\frac{\partial u_e}{\partial \xi} + 2c_{d,l} - H^*\frac{c_{f,l}}{2} \tag{6}
$$

where τ is the pseudo time. Equations (5) and (6) are the fundamental equations of the pseudo-unsteady boundary layer system used in the present work. They consist of a combination of compressible steady terms and incompressible unsteady terms. As such, they cannot be used to model unsteady compressible flows. However, for attached and mildly separated flows around static airfoils, the time-dependent terms become negligible after a long enough time and Eqs. (5) and (6) can be used to model steady-state compressible boundary layer flows. The unsteady terms are only included for relaxation, providing better control over the non-linear convergence; the transient part of the computed response is not considered. Because there are six unknowns, θ, H, H^*, H^{**}, $c_{f,l}$ and $c_{d,l}$ for two equations, closure relations are required to solve the system. The closure relations used in the present method are based on the work of Drela and Giles [1] and Nishida and Drela [7], and are presented in Appendix A, as implemented in BLASTER.

The system is valid for laminar and turbulent flows near equilibrium, when turbulent production and dissipation compensate each other. However, Goldberg [30] provided experimental evidence of significant upstream history effects on Reynolds stresses for turbulent flows featuring an adverse pressure gradient. In these cases, the dissipation coefficient $c_{d,l}$ does not depend only on local flow variables anymore and the Reynolds stress constitutes an additional unknown. To account for this non-equilibrium of the turbulent shear layer, Bradshaw et al. [31] derived a stress-transport equation, used by Green and Brooman [32] to formalize the so-called shear-lag equation where the unknown is the shear-stress coefficient, defined as

$$
C_{\tau_S} = \frac{1}{u_e^2}\left(-\overline{u'v'}\right)_{\max}, \tag{7}
$$

with $\overline{u'v'}$ the Reynolds stress. Ozdemir et al. [5] and Ye [6] have developed unsteady versions of the shear-lag equation for incompressible flow. The equation used here follows very closely the ones used by Ozdemir et al. [5] and Ye [6] but makes use of the modifications brought by Drela and Giles [1]. This leads to the following equation,

$$
\frac{\delta}{U_s u_e C_{\tau_S}}\frac{\partial C_{\tau_S}}{\partial \tau} + \frac{2\delta}{U_s u_e^2}\frac{\partial u_e}{\partial \tau} = -\left(\frac{2\delta}{C_{\tau_S}}\right)\frac{\partial C_{\tau_S}}{\partial \xi} + 5.6\left(C_{\tau_{S\mathrm{EQ}}} - C_{\tau_S}\omega\right) + 2\delta\left(\frac{4}{3H\theta}\left(\frac{c_{f_a}}{2} - \left(\frac{H_k - 1}{6.7 H_k \omega}\right)^2\right) - \frac{1}{u_e}\frac{\partial u_e}{\partial \xi}\right), \tag{8}
$$

where $C_{\tau_{S\mathrm{EQ}}}$ is the equilibrium shear-stress coefficient, H_k the kinematic shape parameter, δ the boundary layer thickness, U_s the equivalent normalized wall slip velocity, all computed using the empirical correlations [1] shown in Appendix A. The factor ω is the dissipation coefficient with $\omega = 1$ on the airfoil and $\omega = 0.9$ in the wake.

Most flows in external aerodynamics feature a transition from a laminar to a turbulent state in a certain region of the boundary layer. The e^N method, presented by Van Ingen [23] and Smith [22], is used to capture the laminar to turbulent transition based on the evolution of disturbances present in a laminar flow. The e^N approach makes use of an amplification ratio $N(\xi)$ whose critical value at transition is taken from experiments. The amplification ratio N is defined as

$$N(\xi) = \ln \frac{A}{A_{\mathrm{crit}}}, \tag{9}$$

where $\frac{A}{A_{\mathrm{crit}}}$ is the ratio between the amplification rate of the perturbation wave triggering transition and a critical amplification rate. With the e^N method, transition occurs when the most unstable Tollmien-Schlichting wave has grown by a given amplification factor. This critical amplification factor depends on the freestream turbulence intensity, defined by Marusic [33] as

$$T_u \equiv \frac{u'}{U}, \tag{10}$$

where u' is the root-mean-square of the turbulent velocity fluctuations and U is the mean flow velocity. The critical amplification ratio N_{crit} can be computed following van Ingen [34]:

$$N_{\mathrm{crit}} = -8.43 - 2.4 \ln (T_u) \, . \tag{11}$$

A common value is $N_{\mathrm{crit}} = 9$ which corresponds to a freestream turbulence intensity of 0.07%. When $N \geq N_{\mathrm{crit}}$, the flow is assumed to become turbulent. For a time-dependent boundary layer, the disturbance growth rate becomes dependent on time,

$$N(\xi, \tau) = N(\mathrm{Re}_\theta(\xi, \tau)), \tag{12}$$

where Re_θ is the Reynolds number based on the momentum thickness. The time-dependence is solely introduced by $\mathrm{Re}_\theta = f(\theta(\xi, \tau))$ in the right-hand side term of Eq. (12). In a steady state, the equation becomes

$$N(\xi) = N(\mathrm{Re}_\theta(\xi)). \tag{13}$$

Taking the derivatives of Eq. (13) with respect to time and to the body-tangential coordinate yields

$$\frac{\partial N}{\partial \tau} = 0, \tag{14}$$

$$\frac{\partial N}{\partial \xi} = \frac{\partial N(\mathrm{Re}_\theta(\xi))}{\partial \xi}. \tag{15}$$

By adding Eq. (14) and (15), a pseudo-unsteady version of the e^N method is obtained,

$$\frac{\partial N}{\partial \tau} + \frac{\partial N}{\partial \xi} = \left(\frac{\mathrm{d}N}{\mathrm{d}\,\mathrm{Re}_\theta} \frac{\mathrm{d}\,\mathrm{Re}_\theta}{\mathrm{d}\xi} \right)_{\text{attached}}. \tag{16}$$

A similar equation was obtained by Ye [6] for unsteady flows. In the present work, the time dependence of Re_θ is neglected. The terms $\frac{\mathrm{d}N}{\mathrm{d}\,\mathrm{Re}_\theta}$ and $\frac{\mathrm{d}\,\mathrm{Re}_\theta}{\mathrm{d}\xi}$ are computed from empirical formulae [26], summarized in Appendix A. A correction term $A_{\text{separated}}$ is added to take into account the effects of separation. The term is obtained from another empirical formula [1], also given in Appendix A. Finally,

$$\frac{\partial N}{\partial \tau} + \frac{\partial N}{\partial \xi} = \left(\frac{\mathrm{d}N}{\mathrm{d}\,\mathrm{Re}_\theta} \frac{\mathrm{d}\,\mathrm{Re}_\theta}{\mathrm{d}\xi} \right)_{\text{attached}} + A_{\text{separated}}. \tag{17}$$

The slope $\mathrm{d}N/\mathrm{d}\xi$ and $A_{\text{separated}}$, which modifies the envelope amplification rate in separated flows, are evaluated following Drela and Giles [1] and Nishida and Drela [7]. It is important to mention that the e^N method is triggered based on the local values of the boundary layer parameters only.

For high Reynolds number flows, a free wake is likely to allow the exponential growth of disturbances, which leads to a rapid breakdown into turbulence. Only turbulent wakes are considered in this work as laminar wakes do not exist in the regimes of interest, as highlighted by Drela [26]. Equations (5), (6) and (8) remain valid in the wake region if terms involving the friction coefficient c_f are ignored. Similarly, all closure relations used in the present method and given in Appendix A remain valid in the wake layer when the wall contribution is ignored (i.e., $c_{f,l} = 0$).

A particular observation should be made for the equilibrium shear stress coefficient, $C_{\tau_{S\mathrm{EQ}}}$. Drela [26] states that the lag Eq. (8) should in principle be modified to reflect the more vigorous mixing processes observed in wakes and the resulting increased dissipation. This is a feature that is generally ignored throughout the literature and only Green and Brooman [32] made such adaptations that are only valid for symmetric wakes. Drela [35] presented an adaptation of this closure relation for the wake in the case of blunt trailing edge airfoils. Even though only sharp trailing edges are considered in the present work, Drela [35]'s adaptation has been retained and has been found to slightly improve the results, when compared to reference results.

The solution obtained after solving Eqs. (5), (6), (8) (17) provides the momentum thickness and shape factor

distributions on the airfoil surface. They are used to compute the displacement thickness of the boundary layer, as

$$\delta^* = \theta H. \tag{18}$$

The displacement thickness is then used to compute the blowing velocity,

$$V_e = \frac{1}{\rho_e} \frac{d(\rho_e u_e \delta^*)}{d\xi}, \tag{19}$$

at the center of gravity of each element on the airfoil surface. The blowing velocity is computed using a second order central finite-difference scheme. The computed blowing velocity is finally used as a boundary condition on the airfoil surface when solving the inviscid flow to account for the presence of the boundary layer.

IV. Coupling strategy

The coupling strategy considered in this work is based on the quasi-simultaneous methodology, in which the boundary layer equations developed in Section III are solved alongside an approximation of the inviscid flow. Veldman [18, 20] proposed a strategy that has the advantages of the fully-simultaneous method and avoids the singularity observed in the separation region. In this method, the boundary layer equations are solved simultaneously with an approximation based on thin airfoil theory, and the velocity at the edge of the boundary layer becomes an unknown of the viscous problem. Veldman proposed a simplified interaction law based on the extensive analysis of Coenen [36] in the form of the algebraic equation

$$\left(u_e - \frac{4U_\infty}{\pi h}\delta^*\right)^{(\text{new})} = \left(u_e - \frac{4U_\infty}{\pi h}\delta^*\right)^{(\text{old})}, \tag{20}$$

where U_∞ is the freestream velocity and h the boundary layer cell size in the tangential direction. Superscripts "new" and "old" denote that the quantity is evaluated at the current and previous coupling iterations, respectively, *i.e.,* u_e^{new} represents the velocity at the edge of the boundary layer computed by the viscous solver at the current viscous-inviscid coupling iteration and u_e^{old} the velocity computed by the inviscid solver at the previous coupling iteration. An unsteady version of Eq. (20) is required since it must be solved simultaneously with the boundary layer model, which is a system of pseudo-time dependent differential equations. Taking the derivatives of Eq. (20) with respect to τ and ξ leads to

$$\left(\frac{\partial u_e}{\partial \tau} - \frac{4U_\infty}{\pi h}\frac{\partial \delta^*}{\partial \tau}\right)^{(\text{new})} = \left(\frac{\partial u_e}{\partial \tau} - \frac{4U_\infty}{\pi h}\frac{\partial \delta^*}{\partial \tau}\right)^{(\text{old})} \tag{21}$$

and

$$\left(\frac{\partial u_e}{\partial \xi} - \frac{4U_\infty}{\pi h}\frac{\partial \delta^*}{\partial \xi}\right)^{(\text{new})} = \left(\frac{\partial u_e}{\partial \xi} - \frac{4U_\infty}{\pi h}\frac{\partial \delta^*}{\partial \xi}\right)^{(\text{old})}. \tag{22}$$

Since the inviscid velocity $u_e^{(\text{old})}$ and the displacement thickness $\delta^{*(\text{old})}$ are steady state solutions obtained at the previous coupling iteration, their time derivatives are zero. Adding Eqs. (21) and (22) yields

$$\left(\frac{\partial u_e}{\partial \tau} - \frac{4U_\infty}{\pi h}\frac{\partial \delta^*}{\partial \tau}\right)^{(\text{new})} + \left(\frac{\partial u_e}{\partial \xi} - \frac{4U_\infty}{\pi h}\frac{\partial \delta^*}{\partial \xi}\right)^{(\text{new})} = \left(\frac{\partial u_e}{\partial \xi} - \frac{4U_\infty}{\pi h}\frac{\partial \delta^*}{\partial \xi}\right)^{(\text{old})}. \tag{23}$$

Using the definition of the boundary layer shape factor $H \equiv \frac{\delta^*}{\theta}$, and defining $\tilde{c} \equiv \frac{4U_\infty}{\pi h}$ [†], the equation becomes

$$\left(\frac{\partial u_e}{\partial \tau} - \tilde{c}\frac{\partial(\theta H)}{\partial \tau} + \frac{\partial u_e}{\partial \xi} - \tilde{c}\frac{\partial(\theta H)}{\partial \xi}\right)^{(\text{new})} + \left(-\frac{\partial u_e}{\partial \xi} + \tilde{c}\frac{\partial(\theta H)}{\partial \xi}\right)^{(\text{old})} = 0. \tag{24}$$

The addition of this equation in the boundary layer model leads to a system of four time-dependent partial differential equations. Equations (5), (6) and (24) are solved in the laminar and turbulent regimes. Equation (17) is solved only in the laminar case and is replaced by Eq. (8) in the turbulent case.

The pseudo-time marching strategy used in this work differs from the literature. Works using an unsteady quasi-simultaneous coupling [5, 6] usually compute time-dependent solutions of the interacting viscous-inviscid flow, whereas only steady-state solutions can be computed within the present work as the steady nature of the inviscid flow model prevents the computation of unsteady flows. Moreover, the time dependence is discarded in the closure models used to solve the flow in the boundary layer. Therefore, the pseudo-unsteady nature of the viscous solver is only used to allow the computation of difficult cases such as highly separated and transonic flows. Figure 2 compares the algorithms of the quasi-simultaneous coupling strategy used in this work (a) and one from the literature (b) [5]. In Fig. 2(a), the viscous-inviscid communication is carried out between steady states and the pseudo-time loop is only associated with the viscous solver. In other words, the time integration of the pseudo-unsteady IBL equations takes place within each coupling iteration and for each streamwise location. On the other hand, a classical unsteady formulation as shown in Fig. 2(b) solves the coupled problem at each time step. As such, it is interesting to mention that the quasi-simultaneous coupling methodology adopted in this study does not require each solver to reach a fully converged steady state at every coupling iteration to obtain a valid solution. In particular, the blowing velocity distribution can be updated between Newton subiterations of the inviscid solver, and, at best, after each iteration. Since the inviscid flow computation typically accounts for more than 99% of the total computational cost, this strategy substantially reduces the overall computational time. However, this methodology may compromise the robustness of the coupling algorithm, particularly for highly lifting cases or at high Mach number. In such cases, intermediate solutions may exhibit oscillatory behavior or develop non-physical gradients that the viscous solver cannot accommodate, potentially leading the coupled algorithm to diverge. Moreover, there is no established guideline for determining the appropriate number of inviscid Newton iterations between consecutive updates of the blowing velocity. In practice, this number of subiterations is left to the user's discretion. For most cases, a single inviscid iteration per coupling step is sufficient to minimize computational

[†]Note that $\tilde{c}^{\text{new}} \neq \tilde{c}^{\text{old}}$ if the cell size h changes between two consecutive iterations.

expense, whereas increasing this number, up to full steady-state convergence at each coupling step, can enhance robustness when required.

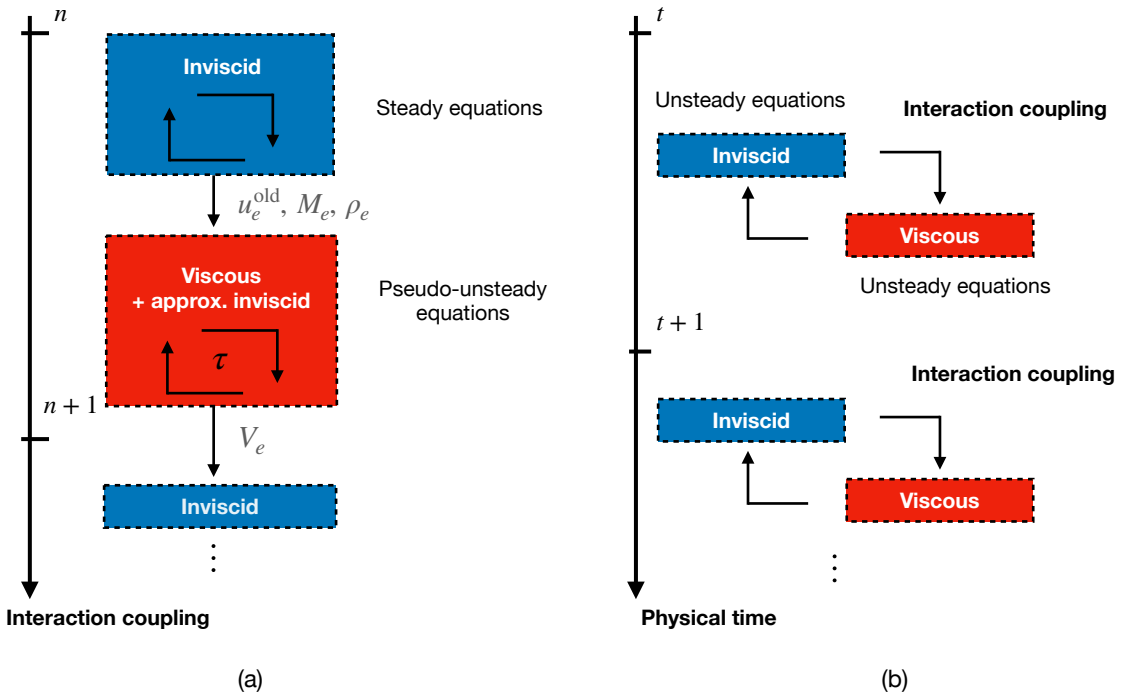

Fig. 2 Pseudo-unsteady quasi-simultaneous coupling proposed here (a) and classical formulation (b) [5]. n **denotes the VII iterations,** t **physical time and** τ **pseudo-time.**

V. Numerical method

A set of partial differential equations along with closure relations have been introduced in the previous sections to characterize a transitional laminar and turbulent boundary layer. The system is composed of Eqs. (5), (6), (17), (24) and (8) with the unknowns θ, H, N, u_e and C_{τ_S}. In the laminar case, $C_{\tau_S} = 0$ and in the turbulent case $N = N_{\text{crit}}$. At each streamwise boundary layer station i, the system of equations is written in the matrix form

$$A(U_i)\frac{\partial U_i}{\partial \tau} + B(U_i, U_{i-1}) = 0, \tag{25}$$

where

$$A(U_i) = \begin{pmatrix} \frac{H}{u_e} & \frac{\theta}{u_e} & 0 & \frac{\theta H}{u_e^2} & 0 \\ \frac{1+H(1-H^*)}{u_e} & \frac{\theta(1-H^*)}{u_e} & 0 & \frac{\theta(2-H^*H)}{u_e^2} & 0 \\ 0 & 0 & 1 & 0 & 0 \\ -\tilde{c}H & -\tilde{c}\theta & 0 & 1 & 0 \\ 0 & 0 & 0 & \frac{2\delta}{U_s u_e^2} & \frac{\delta}{U_s u_e C_{\tau_S}} \end{pmatrix} \tag{26}$$

and

$$B(U_i) = \begin{pmatrix} \frac{\partial \theta}{\partial \xi} + (2 + H - M_e^2)\frac{\theta}{u_e}\frac{\partial u_e}{\partial \xi} - \frac{c_{f,l}}{2} \\ \theta\frac{\partial H^*}{\partial \xi} + (2H^{**} + H^*(1-H))\frac{\theta}{u_e}\frac{\partial u_e}{\partial \xi} - 2c_{d,l} + H^*\frac{c_{f,l}}{2} \\ \frac{\partial N}{\partial \xi} - \left(\frac{\mathrm{d}N}{\mathrm{d}\,\mathrm{Re}_\theta}\frac{\mathrm{d}\,\mathrm{Re}_\theta}{\mathrm{d}\xi}\right)_{\text{attached}} - A_{\text{separated}} \\ \left(\frac{\partial u_e}{\partial \xi} - \tilde{c}\frac{\partial(\theta H)}{\partial \xi}\right)^{(\text{new})} + \left(-\frac{\partial ue}{\partial \xi} + \tilde{c}\frac{\partial(\theta H)}{\partial \xi}\right)^{(\text{old})} \\ \left(\frac{2\delta}{C_{\tau_S}}\right)\frac{\partial C_{\tau_S}}{\partial \xi} - 5.6\left(C_{\tau_{S\text{EQ}}} - C_{\tau_S}\omega\right) - 2\delta\left(\frac{4}{3H\theta}\left(\frac{c_{fa}}{2} - \left(\frac{H_k - 1}{6.7H_k\omega}\right)^2\right) - \frac{1}{u_e}\frac{\partial u_e}{\partial \xi}\right) \end{pmatrix} \tag{27}$$

or in a more convenient way,

$$\frac{\partial U_i}{\partial \tau} + \tilde{F}(U_i) = 0, \tag{28}$$

where $U_i = [\theta, H, N, u_e, C_{\tau_S}]$ at point i and $\tilde{F}(U_i) = A^{-1}B$. The set of equations is stiff because of the behavior of the shape parameter in Eq. (6) near transition. More specifically, on the right-hand side of the equation, the very small quantity θ multiplying the large and rapidly varying gradient $\frac{\partial H^*}{\partial \xi}$ constitutes the main numerical difficulty to overcome. A first-order upwind scheme is chosen here to discretize the equations in space, which prevents the eventual breakdown of the system in the steep gradient regions and ensures increased stability throughout the entire domain,

$$\frac{\partial U_i}{\partial \xi} \approx \frac{U_i - U_{i-1}}{\Delta \xi_i}, \tag{29}$$

where $\Delta\xi_i = \xi_i - \xi_{i-1}$. Equation (28) becomes

$$\frac{\partial U_i}{\partial \tau} + F(U_i, U_{i-1}) = 0. \tag{30}$$

The numerical approach used to solve the partial differential equations is based on the traditional space marching along the airfoil and wake within each viscous-inviscid iteration. Each point on the body surface is treated individually and is advanced in pseudo-time until a steady state is reached, using the solution at the point just upstream, i.e., $i - 1$ as boundary condition. At the stagnation point, a dirichlet boundary condition is imposed following Schlichting and

Gersten [37] and Moran [38],

$$\theta(\xi = 0) = \sqrt{\frac{0.075}{\mathrm{Re}\ \frac{du_e^{\mathrm{old}}}{d\xi}\Big|_{\xi=0}}}, \tag{31}$$

$$H(\xi = 0) = 2.23, \tag{32}$$

$$N(\xi = 0) = 0, \tag{33}$$

$$u_e(\xi = 0) = u_e^{\mathrm{old}}(\xi = 0), \tag{34}$$

$$C_{\tau_S}(\xi = 0) = 0. \tag{35}$$

The laminar closure relations are used at this point to determine the other variables.

The initial condition at each point i is the converged solution obtained at the upstream point $i - 1$. An alternative would be to use the solution obtained at the previous coupling iteration, but it has been found that reusing this solution does not lead to substantial gain in terms of computational cost and can lead to convergence issues. These convergence problems are mainly identified in the transition region, where significant changes are expected from one iteration to the next. The motivation for using a pseudo-time marching strategy is to enhance the stability of the algorithm by providing more control on the numerical procedure and allowing a rapid elimination of the transient part of the flow. A quick convergence towards a steady state solution can be attained by using large values of the time step, which are usually compatible with implicit time integration. Explicit time discretization is at best conditionally stable and usually requires very small time steps, especially in the case of convection-dominated compressible flows [39]. The transient phase is even more rapidly damped if the scheme is very dissipative in time. This motivates the use of the backward Euler scheme to discretize Eq. (30):

$$\frac{U_i^{k+1} - U_i^k}{\Delta\tau} = -F(U_i^{k+1}). \tag{36}$$

The equation is linearized using Taylor expansion, such that

$$\left(\frac{I}{\Delta\tau} + J(U_i^k)\right)\Delta U_i = -F(U_i^k), \tag{37}$$

where I is the identity matrix, $\Delta\tau$ the time step, $J = \frac{\partial F}{\partial U}$ the Jacobian matrix, $\Delta U_i = U_i^{k+1} - U_i^k$ the solution increment at point i and k the number of the time iteration. This linear set of equations is solved using a direct LU method. The Jacobian is computed using second order central finite difference.

The Courant-Friedrichs-Lewy (CFL) number,

$$\mathrm{CFL} = \frac{a_{\mathrm{adv}}\Delta\tau_i}{\Delta\xi_i}, \tag{38}$$

is used to compute the time step $\Delta\tau_i$ at each point i. The advection velocity a_{adv} is given by

$$a_{\text{adv}} = a_{\text{sound}} + u_e, \tag{39}$$

with u_e the inviscid velocity computed by the viscous solver and a_{sound} the speed of sound. The speed of sound is obtained from the isentropic relation

$$a^2_{\text{sound}} = a^2_{\text{sound},\infty} + \frac{\gamma - 1}{2} u^2_\infty - \frac{\gamma - 1}{2} u^2_e. \tag{40}$$

where $a_{\text{sound},\infty}$ is the freestream speed of sound, computed from the definition of the Mach number as $a_{\text{sound},\infty} = u_\infty / M_\infty$, u_∞ the freestream velocity and $\gamma = 1.4$ the heat capacity ratio of air. Obtaining the steady-state solution of the non-linear time dependent system is done by quickly eliminating the transient part through time advancement control. Kelley and Keyes [40] have noted that it is almost impossible to use a large time-step right from the beginning of the simulation, which would correspond to a non-relaxed Newton method. Initial relaxation iterations are usually required to get sufficiently close to the solution for Newton's method to work properly. In this case, success of the initial phase of the time integration is ensured by providing a small enough CFL. As the solution U approaches the steady solution, denoted U^{steady}, the CFL can be increased without breaking down the convergence. In this work, the CFL is adapted by means of the Switched Evolution Relaxation (SER) method [41] and is driven by the evolution of the residuals. More precisely, the CFL at iteration k is given by

$$\text{CFL}^k = \text{CFL}^0 \left(\frac{||R^0||}{||R^{k-1}||} \right)^{0.7}, \tag{41}$$

where R^k is the residual at iteration k, computed from

$$R^k = \left\| F(U^{k+1}) + \frac{\Delta U^k}{\Delta \tau^k} \right\|. \tag{42}$$

In this work, there is no upper bound on the CFL number. Kelley and Keyes [40] showed that for inviscid compressible flows, there is a fairly long induction phase, in which the model is guided towards the Newton convergence domain with relatively small time steps. In the present case of a viscous flow, this induction phase is identified but is limited to a few iterations. The residual tends to stagnate during the first two to three iterations after which the CFL quickly jumps to high values suited for a Newton-like (in the best case quadratic) convergence.

Figure 3 provides a simplified overview of the overall viscous-inviscid interaction algorithm implemented in BLASTER. The schematic describes the different conditions necessary to move from one part to another, indicated by rhombuses, and the main actions taken by the algorithm, represented by rectangles. Modules represented by a red

rectangle are the ones where a non-linear set of equations is solved. More specifically, this figure shows how the main loops on the viscous side are nested, with the coupling loop being the outermost loop which handles the interaction between the viscous and the inviscid solvers. In practice, the upper side is treated first, followed by the lower side and then the wake, as it requires the solution on both airfoil sides as boundary condition. The solution is advanced in the streamwise direction from the boundary condition (stagnation point for both airfoil sides or trailing edge for the wake) in the space marching loop, in which each point is treated individually. The innermost loop corresponds to the pseudo-time marching to solve the pseudo-unsteady system of equations at each individual location, as described in Section III.

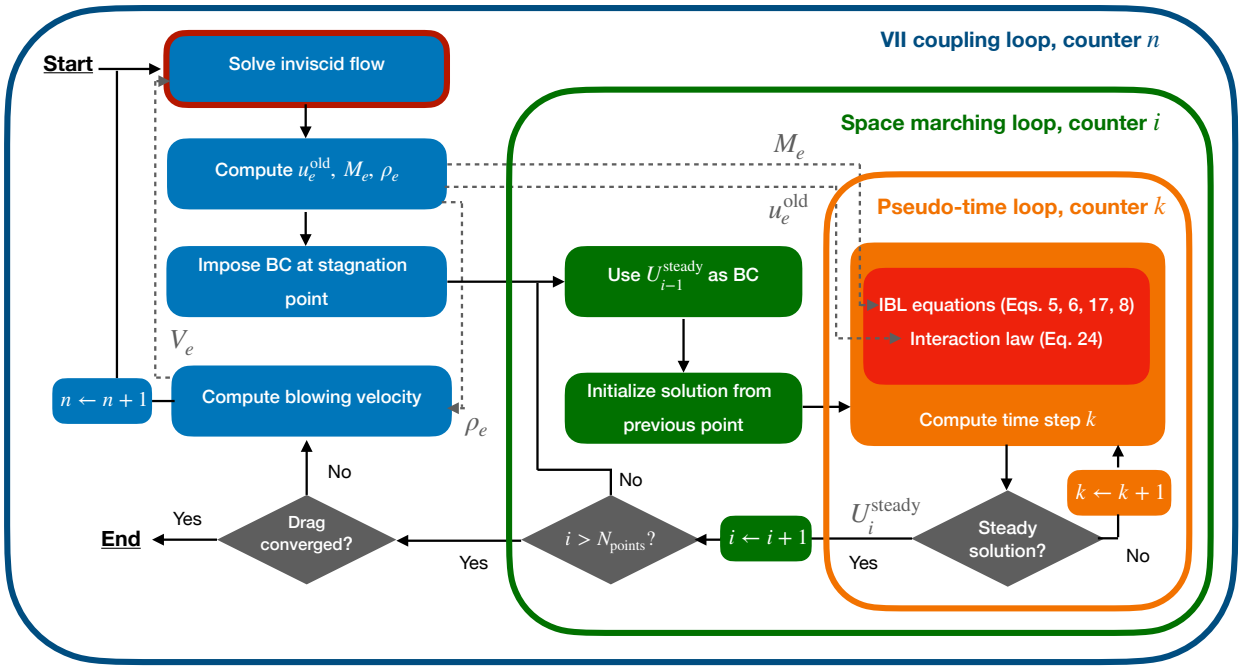

Fig. 3 Diagram of the viscous-inviscid algorithm implemented in BLASTER, where rhombuses denote checks and rectangles represent actions.

VI. Results

Solutions obtained with the coupled integral boundary layer methodology developed in this work and implemented in the free and open-source software BLASTER are presented in this section. Subsonic attached and mildly separated flows at low angles of attack are first considered to validate the implementation. The same case with higher angle of attack is presented to demonstrate the robustness of the present methodology. Transonic capabilities are then demonstrated on four test cases, considering fully-turbulent flows at low incidences and high Mach numbers. BLASTER solutions are obtained on meshes generated using GMSH v4.12.2 [42] with triangular elements and are compared to available experimental measurements. Results for the subsonic configurations are also compared to the VII methodology implemented in XFOIL v.6.99 [4]. XFOIL uses a linear panel method with the Karman-Tsien compressibility correction [43] as an

inviscid flow solver which is not suited for the transonic regime where the flow is subject to non-linear effects introduced by shock waves. RANS and ISES [2] solutions are used as a reference for the transonic test cases. It should be noted that for all the test cases except the highly lifting one, the blowing velocity is updated at each Newton step of the inviscid solver. As a result, a single Newton step of the inviscid solver is computed at each coupling iteration, reducing the computational cost. For the highly lifting case, more numerical stability is required and the inviscid solution is converged to a steady state at each coupling iteration. The initial CFL number used in Eq. (41) is different for each test case and is specified in the corresponding sections.

A. Subsonic attached and mildly separated flows

The flow around the NACA0012 airfoil is modeled in essentially incompressible conditions, with a fixed moderate Reynolds number at multiple angles of attack. The freestream conditions are taken from Gregory and O'reilly [44] and are given in Table 1. The transition is free on both sides of the airfoil. A 10,408-element mesh obtained with GMSH is used for the inviscid calculation, comprising 456 nodes on the surface. The boundary layer stations are defined at these nodes and the inviscid and viscous meshes match on the airfoil surface. The element sizes in the leading and trailing edge regions are 0.1% and 1% of the chord, respectively. A growth ratio of 1.15 is used in the field to determine the mesh size at the farfield boundary, 50 chords away from the airfoil. The initial CFL number is set to 10^3.

Table 1 Freestream parameters used to obtain solutions of subsonic attached or mildly separated flows over the NACA0012 airfoil.

Mach number	0.16
Reynolds number	$2.88 \cdot 10^6$
Angles of attack (°)	0, 2, 4, 6, 8, 10
Airfoil	NACA0012

BLASTER converges in 18, 19, 19, 22, 32 and 128 coupling iterations for each angle of attack depicted in Table 1, respectively. The pressure coefficient on the suction side of the airfoil is presented in Fig. 4 and is compared to the experimental measurements from Gregory and O'reilly [44] and results obtained using XFOIL. Good agreement is observed for each angle of attack. For higher angles of attack, the predictions of the pressure coefficient at the suction peek obtained from BLASTER and XFOIL are slightly different.

The friction coefficient distributions obtained with BLASTER and XFOIL are compared in Fig. 5 for $\alpha = 0°$ and $\alpha = 10°$. There is no available experimental friction coefficient measurement. Both the suction and pressure sides are shown and the laminar to turbulent transition location is visible by the sudden increase in friction. Again, good agreement is observed. For low angle of attack (Fig. 5a), a small difference can be observed in terms of transition prediction. For $\alpha = 10°$ (Fig. 5b), the same transition point and separation bubble in the leading edge region are predicted by both solvers.

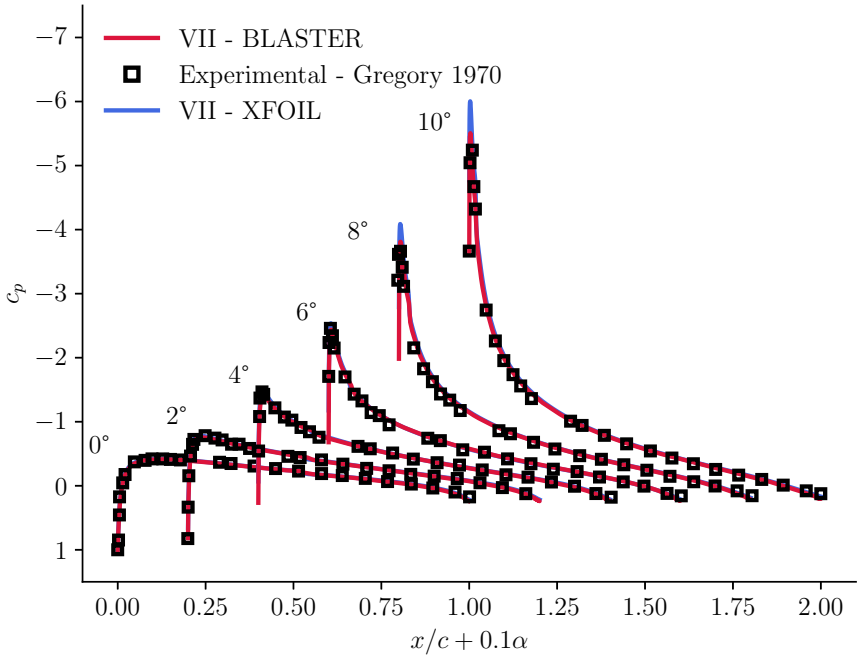

Fig. 4 Pressure coefficient distribution on the suction side of the NACA0012 for the conditions described in Table 1.

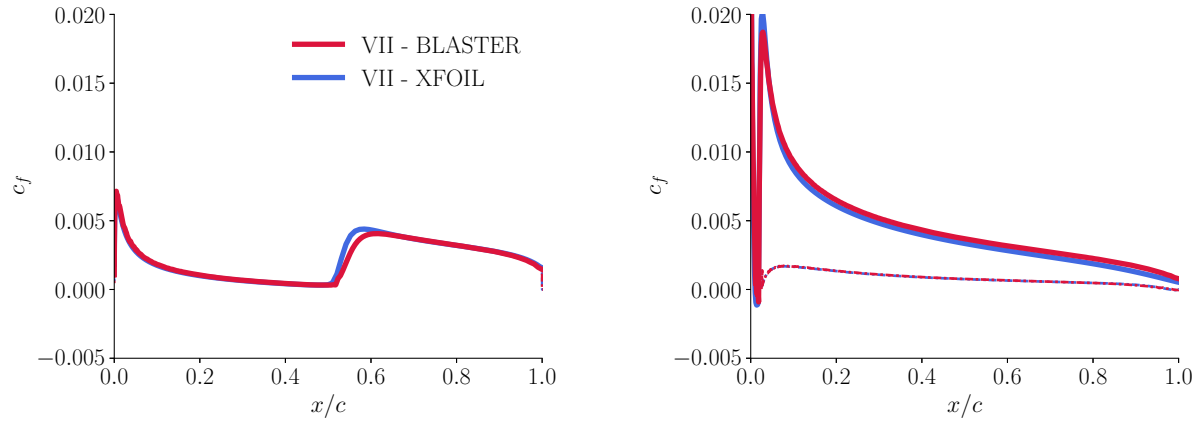

(a) $\alpha = 0°$ (b) $\alpha = 10°$

Fig. 5 Friction coefficient distribution around the NACA0012 airfoil for the conditions described in Table 1. Solid lines show suction side and dashed lines pressure side.

The aerodynamic coefficients predicted by BLASTER and XFOIL are compared in Table 2. The lift coefficient c_l, the drag coefficient $c_{d,\mathrm{SY}}$, computed from Squire and Young [45], and the friction drag coefficient $c_{d,f}$, computed from the integral of c_f on the airfoil surface, are shown. Experimental measurements, obtained at Re = 3 million, gathered

from Abbott and Von Doenhoff [46] are used as reference results[‡]. Overall, good agreement is observed. As the angle of attack increases, the difference in c_l and $c_{d,\mathrm{SY}}$ increases. However, increasing the angle of attack decreases the difference in $c_{d,f}$. This can be identified in Fig. 5 where the c_f distributions of BLASTER and XFOIL are more similar for higher angle of attack.

Table 2 Lift c_l, total drag $c_{d,\mathrm{SY}}$, and friction drag $c_{d,f}$ coefficients. BLASTER results are compared with XFOIL and experimental data [46].

α	c_l			$c_{d,\mathrm{SY}} \times 10{,}000$			$c_{d,f} \times 10{,}000$		
	BLASTER	XFOIL	Abbott	BLASTER	XFOIL	Abbott	BLASTER	XFOIL	Abbott
0	0.000	0.000	0.000	52.1	51.6	59.1	42.6	45.2	-
2	0.227	0.227	0.219	54.2	54.2	59.8	43.1	44.5	-
4	0.457	0.450	0.456	62.7	62.9	65.8	44.9	45.9	-
6	0.666	0.666	0.657	72.9	76.3	77.7	47.0	47.7	-
8	0.934	0.911	0.875	96.2	94.5	91.3	49.4	49.3	-
10	1.152	1.135	1.099	111.7	117.1	115.3	49.5	49.4	-

Viscous effects have been shown to significantly impact the aerodynamic performance of airfoils when the angle of attack is sufficiently high. The same case with a higher angle of attack is presented to demonstrate the ability of the coupling strategy developed in the present work to overcome the numerical difficulties associated with such flows. The freestream conditions are given in Table 1 and the angle of attack is $\alpha = 15°$. At these flow conditions, the flow around the NACA0012 airfoil exhibits a larger separation region around the leading edge.

The solution presented in the following is obtained on a 12,876-element mesh generated with GMSH including 626 boundary layer stations. Because of the large gradients that exist in the leading edge region, a high refinement is used with elements of size 0.05% of the chord. In the trailing edge region, the element size is 0.8% of the chord. In the field, the same growth ratio of 1.15 as for lower angles of attack is used. In contrast with the other test cases, the inviscid solver is here fully converged to a steady state at every coupling iteration. This enhances numerical stability by preventing the viscous solver from being exposed to unphysical intermediate flow states. In this case, the initial CFL number driving the pseudo-unsteady methodology in the viscous solver is set to 1. Convergence of the viscous-inviscid coupled algorithm is obtained when the drag coefficient between two coupling iterations varies by less than 0.01%. For this type of case, mesh independence is not guaranteed, especially when the laminar to turbulent transition is not tripped. If a finer mesh is used, the lift coefficient c_l can vary by up to 2% when using meshes with twice or four times the number of elements. Similarly, if the tolerance of the convergence criterion on the drag coefficient is decreased, the solution can vary and the lift coefficient can change by 3%.

The BLASTER solution is obtained in 26 coupling iterations. Figure 6 shows the pressure coefficient distribution

[‡]The experimental results have been digitized by NASA and are available on the Turbulence Modeling Resource website `https://turbmodels.larc.nasa.gov/naca0012_val.html`, accessed in July 2024

around the NACA0012 with a closer view of the leading edge region. The solution is compared to the experimental data, XFOIL predictions and to the inviscid solution obtained with DART. In these conditions, a laminar boundary layer develops from the stagnation point located at 6% of the chord on the lower side. At 0.5% of the chord on the upper side, a laminar separation bubble forms, followed by a laminar to turbulent transition. A turbulent boundary layer develops further downstream up to the trailing edge. On the pressure side, the flow is laminar and no transition is predicted. In this high angle of attack configuration, the viscous correction is significant on the suction side. While the suction peak predicted by BLASTER is higher than the one measured experimentally, it matches the XFOIL prediction. The friction coefficient distributions predicted by BLASTER and XFOIL are presented in Fig. 7. The laminar to turbulent transition on the upper side is clearly visible by the sudden increase in friction. Flow separation can be identified when $c_f = 0$ and the laminar separation bubble lies where the friction coefficient is negative. Inside the separation bubble, the flow becomes turbulent and the separation region ends. From that point and until the trailing edge, friction decreases in the turbulent shear layer. Good agreement is observed between the BLASTER and XFOIL solutions, especially in terms of transition location prediction and of the maximum friction after the transition.

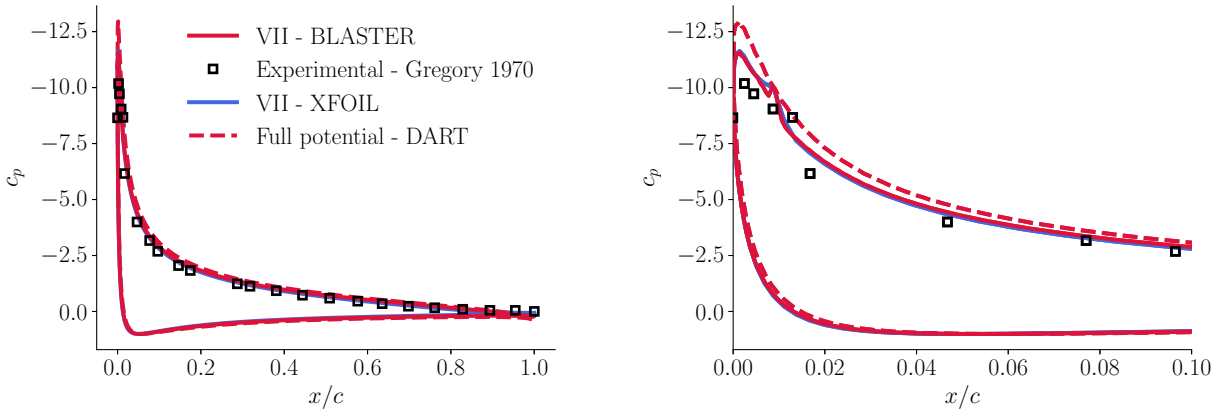

(a) Airfoil.

(b) Leading edge region.

Fig. 6 Pressure coefficient distribution around the NACA0012 at an incidence of 15°.

Unlike the previous cases in attached configurations, the advantage of using a pseudo-unsteady formulation of the IBL problem can be identified in the present limit case. The computation is also performed using the steady state formulation. The solution of the steady formulation of the IBL equations is obtained by solving $B(U_i, U_{i-1}) = 0$, but where vector B is slightly modified from its definition in Eq. 27 by adapting the 4th row so as to use the original interaction law (Eq. (20)) and not our modified version (Eq. (24)). This steady equation is solved iteratively using the same Newton algorithm as for the pseudo-unsteady case but with the adapted Jacobian matrix,

$$\tilde{J}\Delta U = \tilde{B}(U_i, U_{i-1}) \tag{43}$$

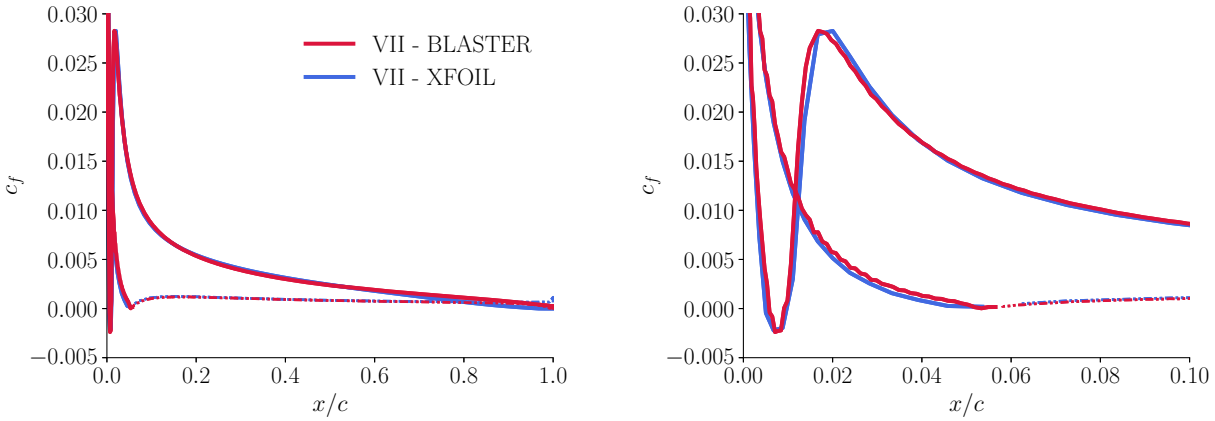

(a) Airfoil.

(b) Leading edge region.

Fig. 7 Friction coefficient distribution around the NACA0012 at an incidence of 15°. Solid lines show suction side and dashed lines pressure side.

where $\tilde{B}$ is the modified matrix B and $\tilde{J}$ is the Jacobian matrix of $\tilde{B}$ with respect to U_i. In this case, several points fail to converge during the first coupling iteration. These points are located upstream and downstream of the separation and in the wake. This can be avoided by using a coarser mesh, but the quantities inside the separation region are not well captured.

B. Transonic flow over the NACA0012 airfoil

The viscous-inviscid interaction methodology developed in this work is now used to predict the transonic flow over a NACA0012 airfoil in the conditions listed in Table 3. These conditions were tested experimentally by McDevitt and Okuno [47]. BLASTER solutions were calculated on a mesh composed of 15, 611 triangular elements. The domain is 50 chords long, the element size on the surface is 0.5% of the chord and a growth ratio of 1.1 was used. The initial CFL number is set to 1. As indicated in the experimental report, transition was not tripped but was observed to occur close to the leading edge in these conditions. For this reason and for the sake of comparison with fully-turbulent RANS solutions, the transition is tripped in the BLASTER simulations and all the boundary layer stations are considered as turbulent. Convergence is obtained when the relative difference of the drag coefficient computed at two successive iterations varies by less than 0.01%.

Table 3 Freestream parameters used for the transonic turbulent flow over the NACA0012 airfoil.

Mach number	0.751
Reynolds number	$9.5 \cdot 10^6$
Angle of attack (°)	1.99
Airfoil	NACA0012

A denser mesh of 38 181 elements was used to assess mesh convergence. The pressure distribution of the inviscid

computation (DART) and the VII solution (BLASTER) obtained on the two meshes is shown in Fig. 8. Although the inviscid solution still varies slightly with the mesh, the viscous solution remains nearly constant. Comparing the friction coefficient distribution on the two meshes shows a similar behavior.

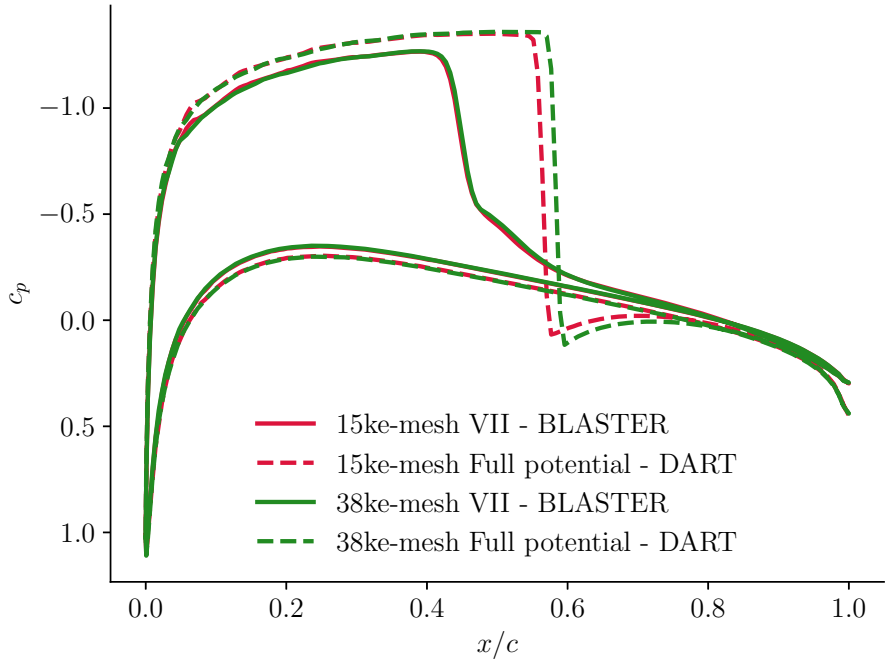

Fig. 8 Mesh convergence of the NACA0012 transonic case. The pressure distributions around the airfoil obtained on two meshes (15 611 and 38 181 elements) are shown.

BLASTER converges in 26 viscous-inviscid iterations and 99.58% of the computational cost is associated with the inviscid calculation. The pressure distribution around the NACA0012 airfoil is shown in Fig. 9 and is compared to the experimental measurements by McDevitt and Okuno [47] and to steady RANS results by Balakumar et al. [48]. The inviscid computation shows a shock wave at 60% of the chord while viscous results predict a weaker shock that lies further upstream. Good agreement is observed between the BLASTER predictions and the reference data.

C. Transonic flow over the RAE2822 airfoil

Three transonic flow configurations over the RAE2822 airfoil are examined, corresponding to case 6, case 9 and case 10 in the experimental database of Cook et al. [49]. These test cases were used by many authors to validate CFD codes [3, 17, 18, 50–53]. More specifically, case 6 and case 9 correspond to attached transonic turbulent flows while case 10 features a boundary layer separation downstream of the shock. The experimental conditions of Mach number and angle of attack have been corrected to account for wind tunnel influence by NASA's NPARC Alliance Verification and Validation Archive for case 6 [54] and by DLR for case 9 and 10 [55]. The corrected flow parameters used in

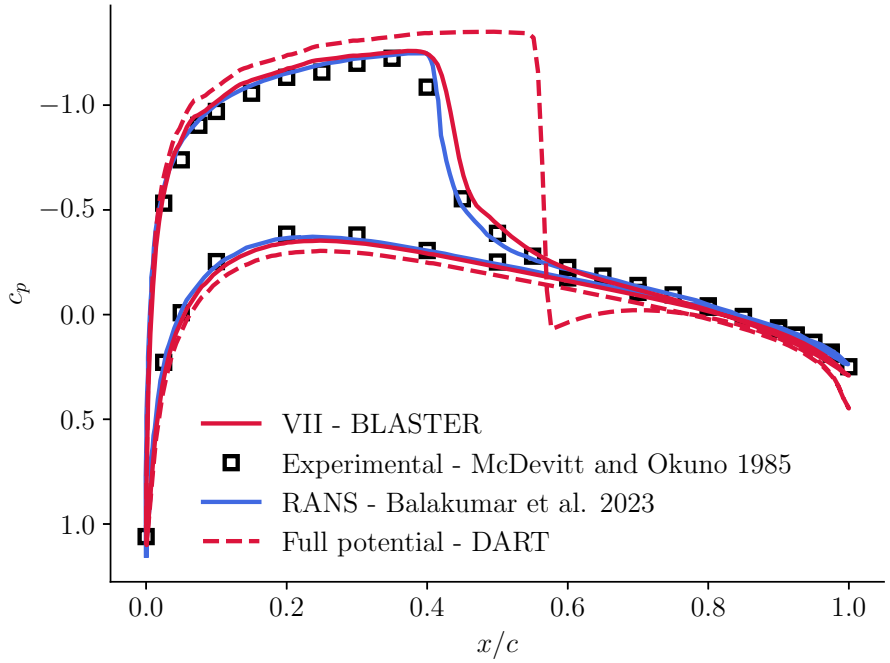

Fig. 9 Pressure coefficient distribution around the NACA0012 for the conditions listed in Table 3.

BLASTER are summarized in Table 4 and are compared to the experimental conditions. The experimental setup was designed such that the transition was tripped at 3% and 10% of the chord on the upper and lower sides, respectively. For case 6 and 9, a 20 169-element mesh is used for the computation with 563 boundary layer stations, which corresponds to element sizes of 0.1% and 0.75% of the chord at the leading and trailing edge, respectively. A growth ratio of 1.1 is used inside the computational domain, long of 50 chords. The domain mesh with a closer view around the airfoil is shown in Fig. 10. For case 10, a slightly coarser mesh was used for robustness reasons. The mesh parameters are the same as for case 6 and 9, except for the trailing edge element size which is set to 1.4%. The initial CFL number is set to 10 for all three cases. Convergence is obtained when the relative difference of the drag coefficient computed at two successive iterations varies by less than 10^{-6}.

Table 4 Freestream parameters for the RAE2822 airfoil flow. Corrections are obtained from NASA [54] for case 6 and DLR [55] for cases 9 and 10.

	Case 6		**Case 9**		**Case 10**	
	BLASTER	Experimental	BLASTER	Experimental	BLASTER	Experimental
Mach number	0.729	0.726	0.730	0.730	0.750	0.750
Reynolds number	$6.5 \cdot 10^6$	$6.5 \cdot 10^6$	$6.5 \cdot 10^6$	$6.5 \cdot 10^6$	$6.2 \cdot 10^6$	$6.2 \cdot 10^6$
Angle of attack (°)	2.31	2.92	2.80	3.19	2.80	3.19

BLASTER results are compared to experimental measurements from Cook et al. [49] and to VII results obtained

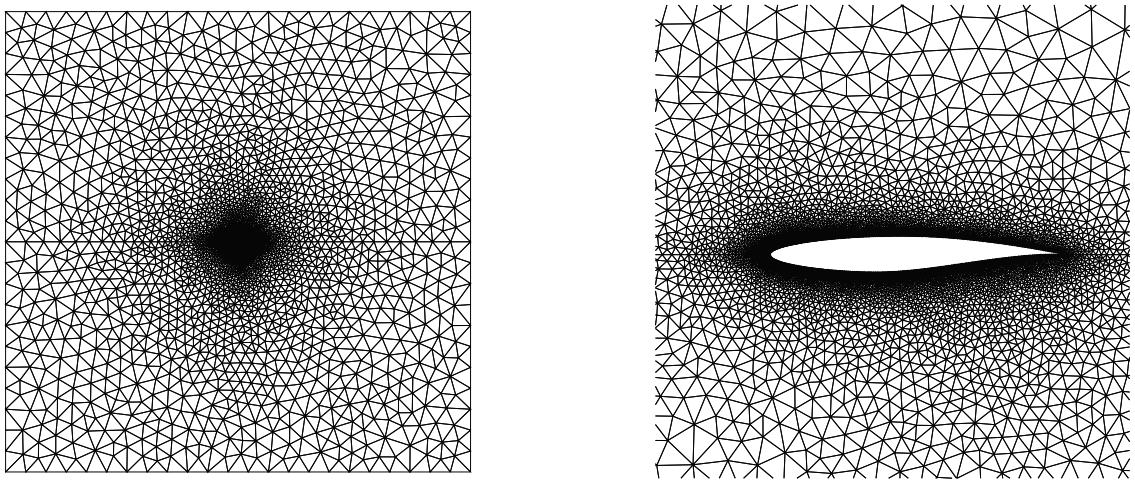

(a) Overall domain (b) Zoom on the airfoil

Fig. 10 Grid used for the computation of the transonic flow around the RAE2822 airfoil using BLASTER.

with ISES [1, 2], which uses a fully-simultaneous coupling strategy with an Euler solver to model the inviscid flow. Both cases are also compared to RANS solutions from the literature by Palacios et al. [50] and to RANS solutions obtained by the present authors using SU^2 [50, 56]. The purpose of these last RANS simulations is to have access to the complete data of the simulations and to compare the friction coefficients with the current VII method. Results have been obtained using SU^2 v7.3.0 on a 52 083-element mesh, depicted in Fig. 11. A circular domain of radius 50-chord was used with an unstructured triangular grid. In the vicinity of the airfoil, quadrangular elements were used to form a boundary layer mesh. The non-dimensional wall distance y^+ of the first cell, defined as

$$y^+ \equiv \frac{u_\star y}{\nu}, \tag{44}$$

where $u_\star = \sqrt{\tau_{Sw}/\rho}$ is the friction velocity and y the distance from the wall in the normal direction, is smaller than 1.4 everywhere on the airfoil. The grid is as similar as possible to the one presented by Palacios et al. [51] but has twice more elements. The solver was configured with the freestream conditions listed in Table 4 and the Spalart-Allmaras turbulence model [57] was used. Palacios et al. [50] used the JST scheme for case 6 and the HLLC scheme for cases 9 and 10. In the present work, all solutions are obtained using the JST scheme to maintain consistency and it was found that this choice had limited impact on the solution and does not alter the comparison. All the remaining numerical settings are the same as the ones used by Palacios et al. [50] and are presented in Table 5.

For these test cases, BLASTER converges after 88, 132, and 63 coupling iterations for cases 6, 9, and 10, respectively. The reduced iteration count for case 10 is attributed to its coarser trailing-edge mesh. The pressure distributions around the airfoil are presented in Fig. 12. Consistent with the NACA0012 results, the strong shock captured in the inviscid solution shifts upstream and weakens once the viscous correction is applied. Overall, the present method demonstrates

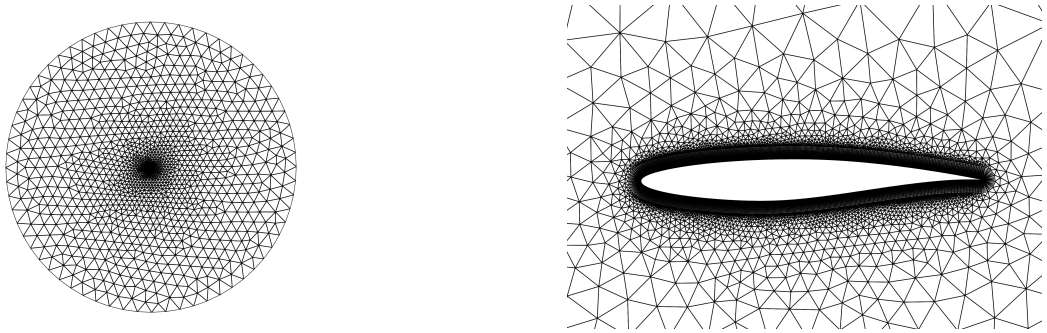

(a) Overall domain (b) Zoom on the airfoil

Fig. 11 Grid used for the computation of the transonic flow around the RAE2822 airfoil using the RANS equations in SU^2.

Table 5 Numerical parameters for the RANS simulation of a transonic turbulent flow over the RAE2822 airfoil with SU^2.

Scheme	JST
Turbulent variables convection	Second-order scalar upwind method
Discretization	Euler-implicit time stepping
Linear solver	GMRES
Limiter	Venkatakrishnan (for upwind schemes)
Convergence criterion	Density: 10^{-10}

good agreement with the reference data, particularly regarding the shock position on the upper surface. On the lower surface, the pressure distribution closely matches the reference solutions.

The distributions of the skin-friction coefficient on the upper surface of the RAE2822 airfoil are presented in Fig. 13, alongside available experimental data, ISES solutions, and the authors' RANS results. For cases 6 and 9, good agreement is obtained, particularly in the vicinity of the shock and further downstream. Case 10 exhibits similarly overall good agreement, with a boundary layer separation predicted downstream of the shock at approximately 60% of the chord. The extent of this separation is well captured, as the predicted reattachment point aligns closely with the reference results. The severity of the separation is comparable to that of the ISES solution but slightly less pronounced than in the RANS results, likely due to the shock being located further downstream in the latter. The main limitation of the BLASTER solution lies in the small oscillations observed in the trailing-edge region. These oscillations become more pronounced with mesh refinement, ultimately preventing convergence of the algorithm when a finer mesh is employed. Nonetheless, their amplitude remains small in the skin-friction coefficient, and they do not significantly affect the computation of the aerodynamic coefficients. It should be noted that with the mesh described above, the coupled solution obtained for case 10 is converged. The discrepancies observed near the leading edge among the various methods, and across the three cases, arise from differences in the laminar-turbulent transition modeling. The RANS simulation does not include a transition model while BLASTER and ISES solutions where obtained by tripping the transition locations in accordance

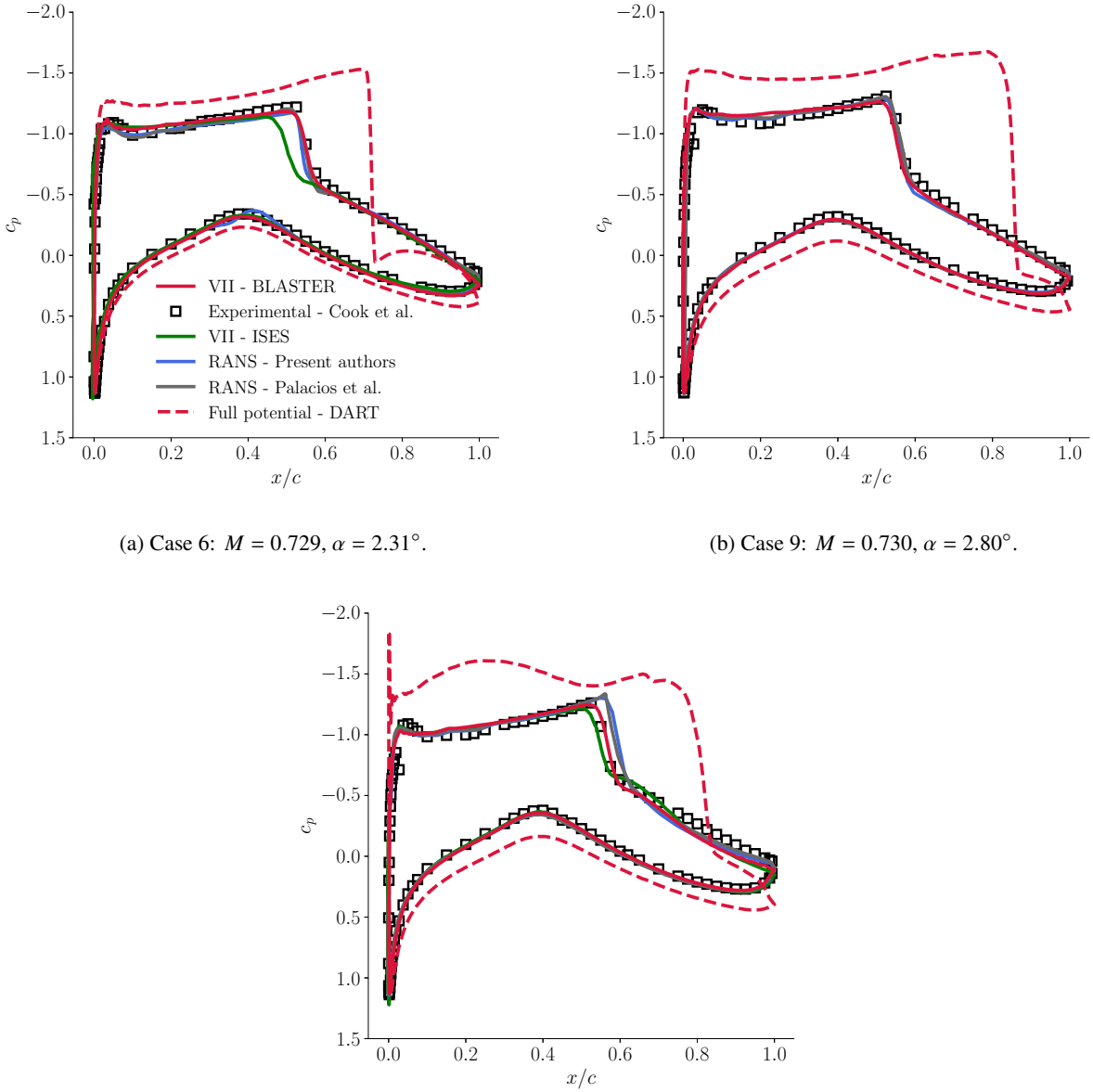

(a) Case 6: $M = 0.729$, $\alpha = 2.31°$.

(b) Case 9: $M = 0.730$, $\alpha = 2.80°$.

(c) Case 10: $M = 0.750$, $\alpha = 2.80°$.

Fig. 12 Pressure coefficient distributions around the RAE2822 for the conditions listed in Table 4.

with the experimental setup, at 3% and 10% of the chord on upper and lower sides, respectively.

Integral boundary layer quantities are now compared to available experimental measurements and available numerical results from ISES on the upper side of the RAE2822. Figs. 14, 15 and 16 show the shape factor H, the displacement thickness δ^* and the momentum thickness θ of the boundary layer along the chord for case 6, 9 and 10, respectively. Overall, good agreement is observed on all cases, especially downstream of the shock location. The same conclusions as the ones discussed for the friction coefficient can be drawn here. A good match is observed for case 6 and 9, while

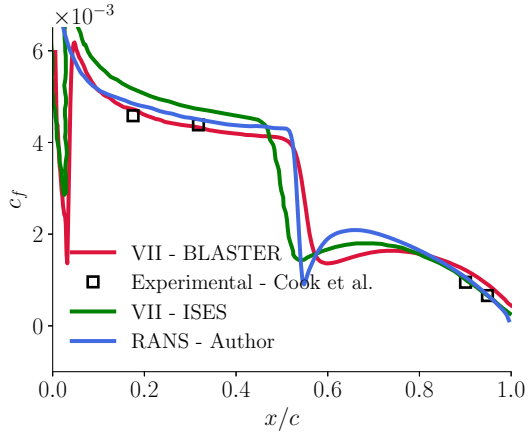

(a) Case 6: $M = 0.729$, $\alpha = 2.31°$.

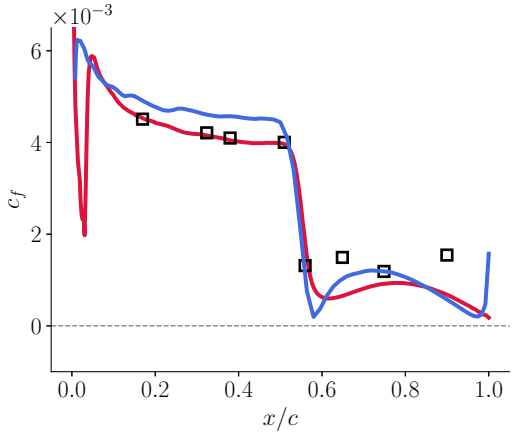

(b) Case 9: $M = 0.730$, $\alpha = 2.80°$.

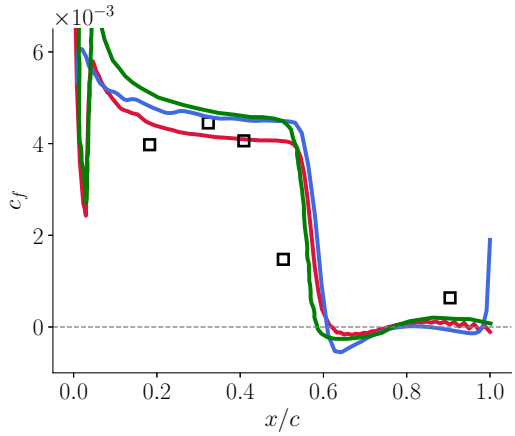

(c) Case 10: $M = 0.750$, $\alpha = 2.80°$.

Fig. 13 Friction coefficient distributions on the upper side the RAE2822 for the conditions listed in Table 4.

the results for case 10 show some oscillations in the trailing edge region.

Table 6 compares the aerodynamic coefficients computed by each method for the three cases. It is clear that the viscous correction applied to the inviscid solution is of great importance in this case. For all cases, the inviscid flow solution overpredicts the lift and the drag, compared to the experimental measurements while corrected results reduce this difference to a few percents. The overprediction of the viscous solution is most likely due to the fact that the pressure on the upper side is slightly underpredicted in the supersonic region, as can be seen in Fig. 12. For case 10, a similar trend is observed with a lift overpredicted by 100% and a drag overpredicted by 73% in the inviscid case, while BLASTER reduces these differences to 1.2% and 1.7%, respectively. The computational cost of each method is also reported in Table 6. The RANS simulations are three orders of magnitude more expensive than BLASTER, which itself is less than one order of magnitude more expensive than the inviscid solver alone. This highlights the efficiency of the present approach to compute transonic turbulent flows around airfoils. It should be noted that the low computational cost of BLASTER is strongly related to the fact that the blowing velocity is updated at each Newton iteration of the

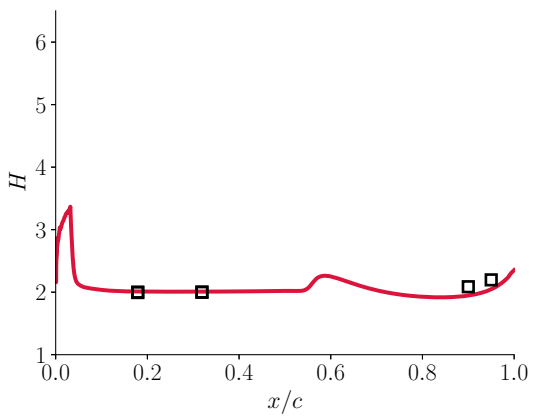

(a) Case 6: $M = 0.729$, $\alpha = 2.31°$.

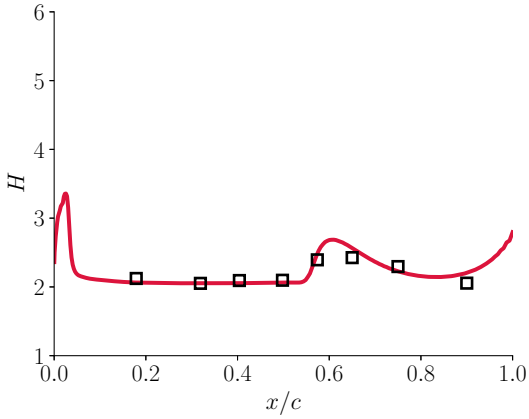

(b) Case 9: $M = 0.730$, $\alpha = 2.80°$.

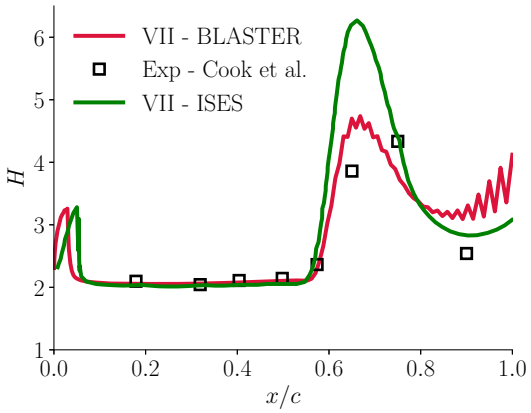

(c) Case 10: $M = 0.750$, $\alpha = 2.80°$.

Fig. 14 Shape factor of the boundary layer distributions on the upper side of the RAE2822 for the conditions listed in Table 4.

inviscid solver. If the inviscid solver reaches convergence at each coupling iteration, the total computational cost is increased to two minutes in these cases.

D. Comparison of the steady and pseudo-unsteady formulations

The test cases shown above demonstrate that the pseudo-unsteady boundary layer formulation developed here can handle a wide range of flight regimes, including high-lift conditions with separation bubbles and transonic flows with shocks and shock-induced separations. This covers most of 2D aerodynamic conditions except for supersonic flows, which are beyond the scope of the present work. In this section, a more detailed comparison between the classical steady and the novel pseudo-unsteady formulations is presented. To compare the two formulations, two representative cases are examined, the NACA0012 airfoil at low incidence highlights the higher computational cost of the pseudo-unsteady method, while the RAE2822 case 9 illustrates its improved robustness in a more complex case.

The flow around the NACA0012 airfoil at an angle of attack of 2° is considered (see Table 1). The same mesh

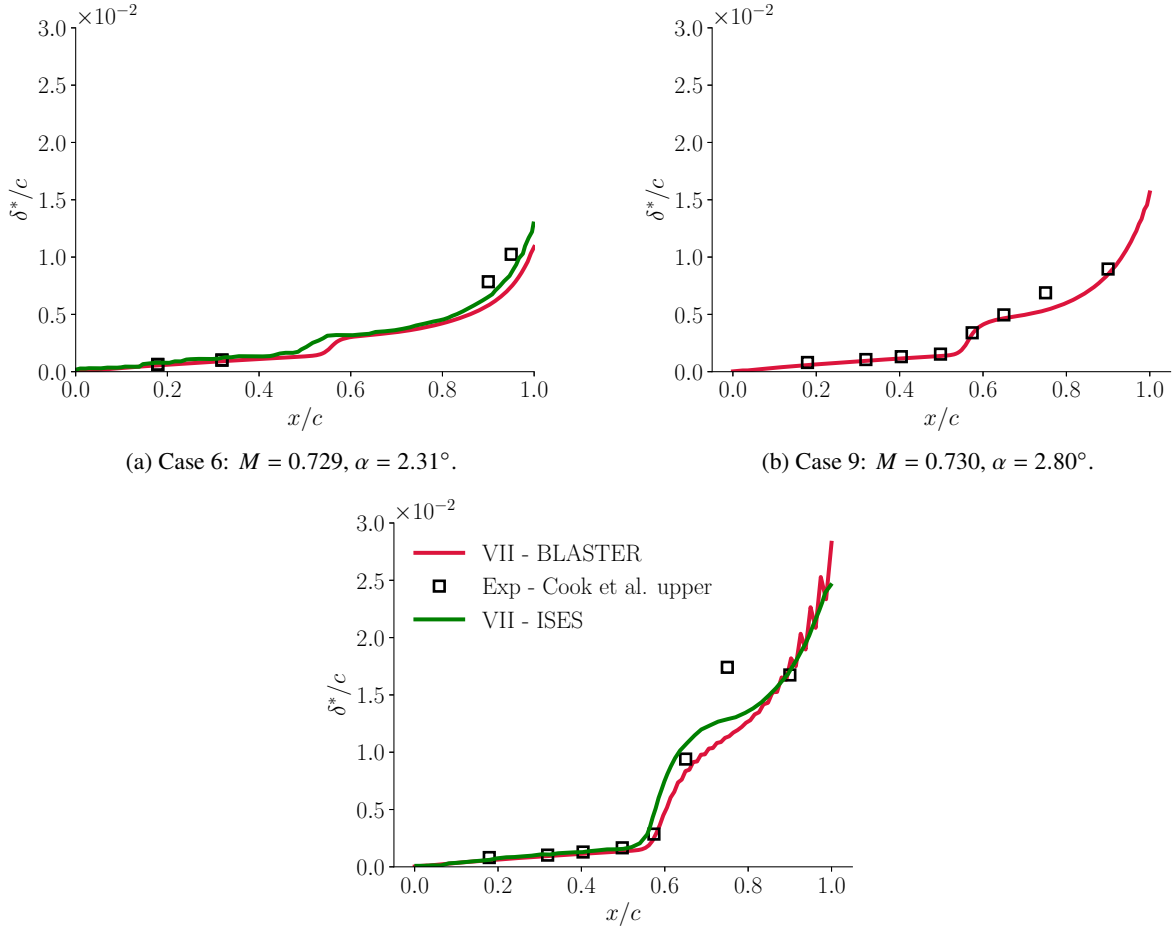

(a) Case 6: $M = 0.729$, $\alpha = 2.31°$.

(b) Case 9: $M = 0.730$, $\alpha = 2.80°$.

(c) Case 10: $M = 0.750$, $\alpha = 2.80°$.

Fig. 15 Displacement thickness distributions on the upper side of the RAE2822 for the conditions listed in Table 4.

is used with 456 boundary layer stations but the convergence criterion on the drag coefficient is tightened to 10^{-8} to increase the number of iterations and obtain a better comparison of the computational costs. The solution of the steady formulation of the IBL equations is obtained by solving $B(U_i, U_{i-1}) = 0$, but where vector B is slightly modified from its definition in Eq. 27 by adapting the 4th row so as to use the original interaction law (Eq. (20)). The same Newton algorithm as for the pseudo-unsteady case is used to solve the equations but with the adapted Jabobian matrix (see Eq. (43)). In the steady computation, all the time-step related operations, i.e., CFL adaptation and construction of the matrix $I/\Delta\tau$, are omitted. Both formulations converge to identical steady solutions during each coupling iteration as shown in Fig. 17a where the evolutions of the lift and drag coefficients during the VII coupling iterations are presented. Figure 17b shows the computational cost of the viscous solver for the entire VII computation as a function of the initial CFL number (CFL^0) used to start the computation. The steady formulation exhibits constant cost, while the pseudo-unsteady cost decreases with increasing initial CFL. For $\text{CFL} \geq 10^4$, its cost approaches that of the steady

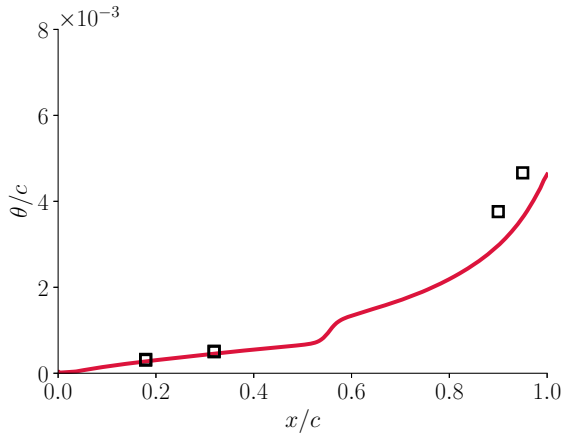

(a) Case 6: $M = 0.729$, $\alpha = 2.31°$.

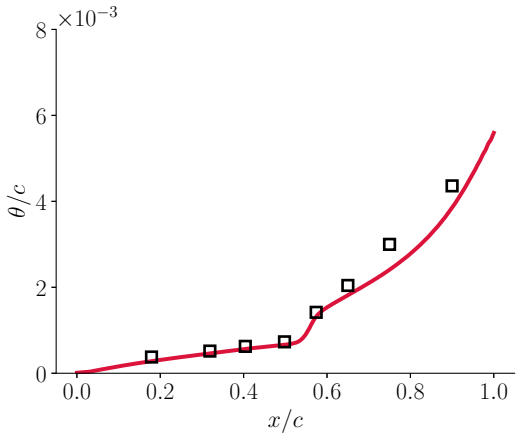

(b) Case 9: $M = 0.730$, $\alpha = 2.80°$.

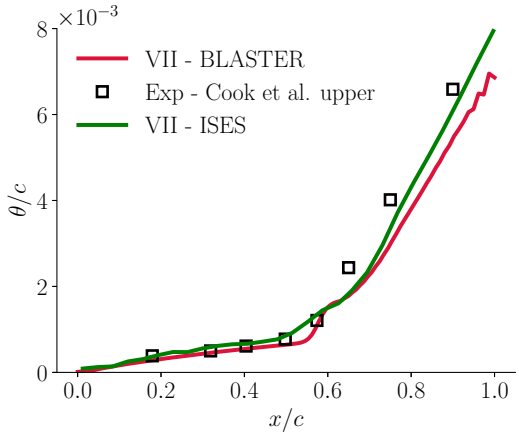

(c) Case 10: $M = 0.750$, $\alpha = 2.80°$.

Fig. 16 Momentum thickness distributions on the upper side of the RAE2822 for the conditions listed in Table 4.

formulation, with a difference of 0.03s, corresponding to 1% of the total computational cost (inviscid + viscous), due to adaptive time-stepping operations. This shows that when both formulations converge, the pseudo-unsteady method can be nearly as efficient as the steady one. Figure 17c compares the convergence of the non-linear viscous iterations for the pseudo-unsteady formulation with varying initial CFL numbers, CFL^0, and the steady formulation. Convergence is shown for the first point downstream of the stagnation point on the upper surface, during the first coupling iteration. This point is selected since its boundary and initial conditions are identical across methods, as the upstream stagnation point conditions remain the same. The steady formulation converges in 7 iterations to a normalized residual norm of 10^{-8}. With a low initial CFL of 100, the pseudo-unsteady formulation requires 19 iterations, showing a slow decay in residuals during the transient part for the first 10 iterations before achieving the expected quadratic convergence because of the adaptive CFL strategy. For higher initial CFL numbers, the pseudo-unsteady convergence approaches that of the steady case, requiring 10 iterations for $\text{CFL}^0 = 10^3$ and 6 iterations for $\text{CFL}^0 = 10^6$ and $\text{CFL}^0 = 10^{10}$. Thus, the

Table 6 Aerodynamic coefficients comparison between the present method, experimental measurements [49], VII results from ISES [2] and RANS results.

	c_l	$c_d \times 10,000$	CPU time
VII BLASTER	0.723	128.4	0m6.2s
Experimental	0.743	127.0	-
VII ISES	0.723	127.0	-
RANS	0.724	140.2	27m59s
Inviscid DART	1.067	178.9	0m2s

Case 6

	c_l	$c_d \times 10,000$	CPU time
VII BLASTER	0.821	174.5	0m11.5s
Experimental	0.803	175.0	-
VII ISES	-	-	-
RANS	0.808	177.4	61m32s
Inviscid DART	1.481	605.3	0m3s

Case 9

	c_l	$c_d \times 10,000$	CPU time
VII BLASTER	0.752	246.2	0m5.0s
Experimental	0.743	242.0	-
VII ISES	0.733	224.0	-
RANS	0.772	295.6	64m8s
Inviscid DART	1.488	419.4	0m7s

Case 10

pseudo-unsteady formulation can match the steady convergence rate when a sufficiently high initial CFL is used, while a lower CFL may be advantageous in more challenging flow cases.

The RAE2822 case 9 (see Table 4) represents a more demanding test case than the subsonic flow case around the NACA0012. The strong shock predicted by the inviscid solution, as seen in Fig. 12b, makes this case particularly challenging, causing the steady formulation to fail to converge. The pseudo-unsteady formulation achieves convergence for sufficiently low initial CFL numbers. As illustrated in Fig. 18, when the initial CFL number exceeds 10^2, the pseudo-unsteady formulation also fails to converge.

VII. Conclusion

This work presents a coupled boundary layer methodology. An inviscid full-potential flow solver, designed for transonic flow computations, is employed to obtain the flow around two-dimensional geometries. This inviscid solution is then used in a boundary layer model based on the integral boundary layer equations. The viscous-inviscid coupling is based on the quasi-simultaneous approach, where the boundary layer equations are solved alongside an approximation of the inviscid flow. The primary innovation introduced in this work is the use of a pseudo-unsteady version of the boundary layer model to achieve steady-state solutions. Additionally, the classical algebraic interaction law used to model the inviscid flow is modified into a pseudo-unsteady partial differential equation. The two-equation model is adapted to its unsteady version with minor adjustments, while closure relations are considered without time dependence. The proposed technique can represent both laminar and turbulent flows, utilizing the unsteady shear-lag equation to

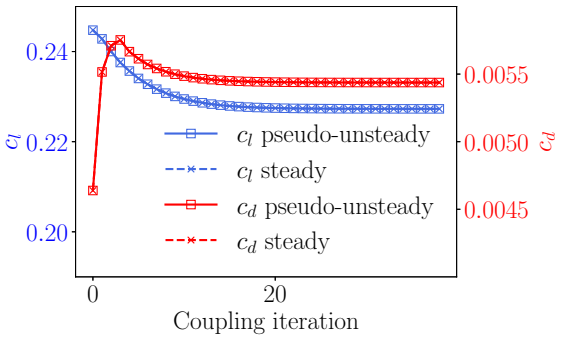

(a) Convergence of the VII algorithm.

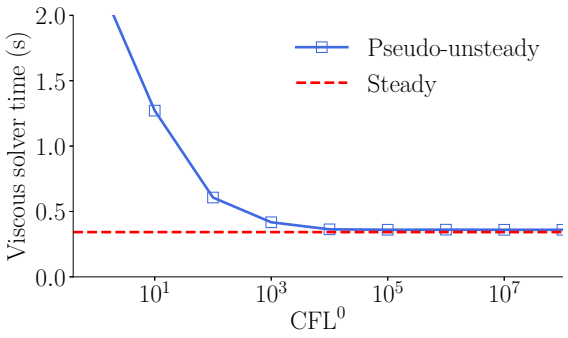

(b) Computational cost vs CFL number.

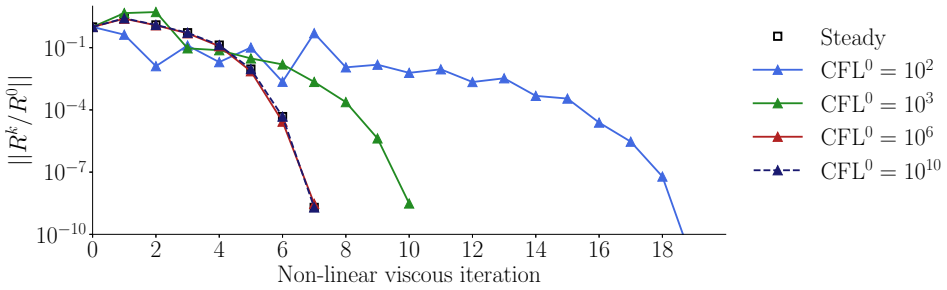

(c) Convergence of the non-linear viscous iterations for the first point downstream of the stagnation point.

Fig. 17 Comparison between the pseudo-unsteady and steady approaches for the NACA0012 airfoil case in Table 1 at an angle of attack of 2°.

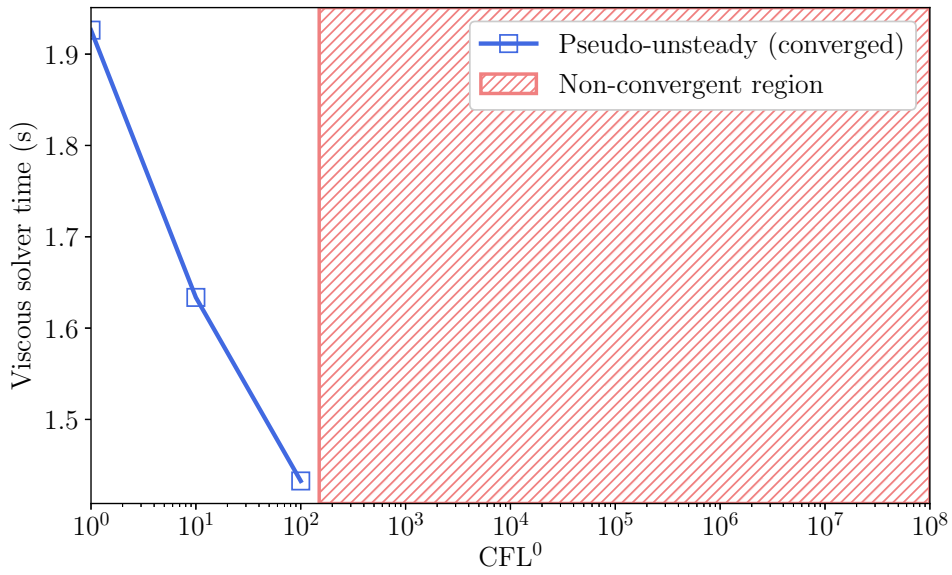

Fig. 18 Computational cost of the viscous solver vs CFL number for the RAE2822 case 9 referenced in Table 4.

characterize turbulent flows in non-equilibrium. Additionally, a pseudo-unsteady version of the e^N method is used to model the laminar-to-turbulent transition in the shear layer. The solution of the boundary layer flow is obtained with a

space marching technique where the solution at the upstream point is used as a boundary condition to compute the spacial gradient. Implicit time integration is used at each spatial station along the airfoil to solve the pseudo-unsteady system with a damped-Newton method until a steady state is reached. It is shown that the pseudo-unsteady version of the boundary layer model enhances the convergence characteristics of the method compared to the steady version using the same coupling strategy. Higher angles of attack, and thus more severe separation cases, as well as higher freestream Mach numbers in transonic flows, could be successfully computed. Results in subsonic configurations have been obtained on the NACA0012 airfoil and compared to experimental data typically used for CFD software validation as well as XFOIL. Transonic capabilities have been shown on the NACA0012 and the RAE2822 airfoils. The pressure and friction coefficients have been compared to experimental measurements and to RANS solutions. A general good agreement has been observed between the proposed VII methodology and the reference data for the pressure and friction coefficient distributions, but also for other boundary layer quantities. Despite small discrepancies in the supersonic region and in the vicinity of the shock for the RAE2822 airfoil, the proposed VII method achieves similar accuracy to RANS approaches but at a fraction of the cost, around 0.5% for the transonic cases presented in this work.

Although the pseudo-unsteady formulation provides more robustness for transonic flows and mild separations at high angle of attack, the approach still faces some limitations. First, remaining convergence difficulties have been observed in limit cases when the mesh spacing is very fine in the trailing edge region, leading to divergence of the coupling algorithm. As a result, a certain degree of dependence on the mesh is observed, especially in highly lifting cases. Nonetheless, the mesh sizes used in the present test cases are sufficient to ensure accurate results. These problems are currently under investigation in order to further improve the capabilities of the method. Secondly, low Reynolds number computations with separating boundary layers still face difficulties in convergence. This limitation could potentially be addressed by considering an inverse coupling strategy. Third, a full parallelization of the algorithm is not possible because of the space marching algorithm. However, the parallelization of the inviscid solver only (as done here) is in practice sufficient in view of the insignificant computational cost of the viscous solver.

Future work will focus on further enlarging the range of applicability of the method, extending it to three-dimensional cases using a strip-based approach [3], under development in BLASTER using the method described by Dechamps et al. [58], and developing a coupled VII adjoint solver for optimization.

A. Closure models

Closure models required to solve the integral boundary layer equations are presented here. Given that only steady solutions are sought, the empirical correlations do not account for time dependent effects. Most of the correlations are taken from Drela and Giles [1] and Nishida and Drela [7]. Some correlations are taken from the source code of XFOIL v6.99 [4].

A. Boundary layer closure relations

The parameters to be modeled are $H^\star, H^{**}, c_{f,l}$ and $c_{d,l}$ and, following Drela and Giles [1], the following depencies are assumed,

$$\begin{aligned} c_{f,l} &= F\left(H_k, M_e, \mathrm{Re}_\theta\right); \\ c_{d,l} &= F\left(H_k, M_e, \mathrm{Re}_\theta\right); \\ H^\star &= F\left(H_k, M_e, \mathrm{Re}_\theta\right); \\ H^{\star\star} &= F\left(H_k, M_e\right). \end{aligned} \tag{45}$$

The kinematic shape parameter, H_k, is obtained from Whitfield [15] as

$$H_k = \frac{H - 0.290M_e^2}{1 + 0.113M_e^2}. \tag{46}$$

while Re_θ is the Reynolds number based on the momentum thickness θ,

$$\mathrm{Re}_\theta = \frac{\rho_e u_e \theta}{\mu_e}. \tag{47}$$

These dependencies depend on the flow state, i.e., whether the boundary layer is laminar or turbulent, as described below.

1. Laminar boundary layer

In a steady incompressible laminar flow, the velocity profile is similar to the Falkner-Skan profile [59]. The kinetic energy shape parameter is expressed locally, but differently whether the flow is attached or detached:

$$H^\star = \begin{cases} 1.528 + 0.0111\frac{(H_k-4.35)^2}{H_k+1} - 0.0278\frac{(H_k-4.35)^3}{H_k+1}, & \\ \quad -0.0002\left[\left(H_k - 4.35\right)H_k\right]^2, & H_k < 4.35, \\ 1.528 + 0.015\frac{(H_k-4.35)^2}{H_k}, & H_k \geq 4.35, \end{cases} \tag{48}$$

For compressible flow, a correction on $H^\star$ is required:

$$H^\star = \frac{H^\star + 0.028M_e^2}{1 + 0.014M_e^2}. \tag{49}$$

The density shape parameter, $H^{\star\star}$, is a corrected kinematic shape parameter only defined for a compressible flow. It is obtained using the correlation

$$H^{**} = \left(\frac{0.064}{H_k - 0.8} + 0.251\right)M_e^2. \tag{50}$$

A normalized local friction coefficient, defined as

$$\overline{c_{f,l}} = c_{f,l}\frac{\mathrm{Re}_\theta}{2}, \tag{51}$$

can be obtained using

$$\overline{c_{f,l}} = \begin{cases} \frac{1}{2}\left[-0.07 + 0.0727\frac{(5.5-H_k)^3}{H_k+1}\right], & H_k < 5.5, \\ \frac{1}{2}\left[-0.07 + 0.015\left(1 - \frac{1}{H_k-4.5}\right)^2\right], & H_k \geq 5.5. \end{cases} \tag{52}$$

The same procedure is applied to the dissipation coefficient, with

$$\overline{c_{d,l}} = 2\,\mathrm{Re}_\theta\,\frac{c_{d,l}}{H^\star}, \tag{53}$$

where

$$\overline{c_{d,l}} = \begin{cases} 0.207 + 0.00205\,(4 - H_k)^{5.5}, & H_k < 4, \\ 0.207 - 0.0016\frac{(H_k-4)^2}{1+0.02(H_k-4)^2}, & H_k \geq 4, \end{cases} \tag{54}$$

without compressibility corrections on $c_{f,l}$ or $c_{d,l}$.

The boundary layer thickness δ, used in Equation(8), is given by

$$\delta = \theta\left(3.15 + H + \frac{1.72}{Hk - 1}\right). \tag{55}$$

The shear stress coefficient at equilibrium, $C_{\tau_{S_{\mathrm{EQ}}}}$, is always zero in the laminar part of the boundary layer.

2. Turbulent boundary layer

In the case of a turbulent boundary layer, the self-similarity assumption is not valid. Nishida and Drela [7] suggests to start from an expression of the skin friction coefficient:

$$F_c c_{f,l} = \frac{0.3\mathrm{e}^{-1.33H_k}}{\left(\frac{\ln \mathrm{Re}_\theta}{2.3026}\right)^{-1.74-0.31H}} + 0.00011\left[\tanh\left(4 - \frac{H_k}{0.875}\right) - 1\right], \tag{56}$$

where $F_c = \sqrt{1 + 0.2M_e^2}$. This particular expression of F_c is given by Drela and Giles [1] and is used to compute subsonic and transonic flow solutions. The kinetic energy shape parameter is defined as

$$H^\star = \begin{cases} 1.5 + \frac{4}{\mathrm{Re}_\theta} + \left(0.5 - \frac{4}{\mathrm{Re}_\theta}\right)\left(\frac{H_0-H_k)}{H_0-1}\right)^2\left(\frac{1.5}{H_k+0.5}\right), & H_k < H_0, \\ 1.5 + \frac{4}{\mathrm{Re}_\theta} + (H_k - H_0)^2\left[\frac{0.007\ln \mathrm{Re}_\theta}{\left(H_k - H_0 + \frac{4}{\ln \mathrm{Re}_\theta}\right)} + \frac{0.015}{H_k}\right], & H_k \geq H_0, \end{cases} \tag{57}$$

with

$$H_0 = \begin{cases} 3 + \frac{400}{\mathrm{Re}_\theta}, & \mathrm{Re}_\theta \geq 400, \\ 4, & \mathrm{Re}_\theta < 400. \end{cases} \tag{58}$$

The density shape parameter is defined as

$$H^{**} = \left(\frac{0.064}{H_k - 0.8} + 0.251 \right) M_e^2. \tag{59}$$

Lastly, a correlation for the dissipation coefficient is required. The work of Green and Brooman [32], among others, shows that if turbulent production and dissipation are in near equilibrium, $c_{d,l}$ depends only locally on the turbulent shear layer's parameters. This equilibrium is usually assumed in most algebraic turbulence models. However, Goldberg [30] provided experimental evidence of significant upstream history effects on Reynolds stresses for flows demonstrating an adverse pressure gradient. In such scenario, it is clear that an empirical correlation for the dissipation coefficient can not be obtained easily. Following Thomas [60] and LeBalleur [61], the method consists in separating the contributions to the dissipation coefficient between the local wall layer contribution and the upstream effect, each being defined by a velocity and a stress scale. Introducing the equivalent normalized wall slip velocity,

$$U_s = \frac{H^\star}{2} \left(1 - 4 \left(\frac{H_k - 1}{3H} \right) \right), \tag{60}$$

the dissipation coefficient is expressed as

$$c_{d,l} = \frac{c_{f,l}}{2} U_s + C_{\tau_S} (1 - U_s). \tag{61}$$

The wall contribution from the wall layer, i.e., the first term of the right hand side, driven by $c_{f,l}$, is determined strictly by the local boundary layer. The second term of the right hand side is driven by the shear stress coefficient C_{τ_S} and is influenced by upstream conditions in the turbulent shear layer, obtained by solving Eq. (8).

The boundary layer thickness δ in the turbulent portion of the boundary layer is computed following the same closure relation as in the laminar boundary layer, Eq. (55). The equilibrium shear-stress coefficient is computed following

$$C_{\tau_{S\mathrm{EQ}}} = \sqrt{H^* \tilde{C} \frac{(H_k - 1)(H_k - 1 - \frac{18}{\mathrm{Re}_\theta})}{(1 - U_s) H_k^2 H}} \tag{62}$$

where $\tilde{C} = \frac{0.5}{6.7^2 \times 0.75} \sim 0.01485$ is a constant.

B. Empirical formula of the transition model

The slopes of the e^N method for attached flow in Eq. (16) are taken from Drela [26]. Successively,

$$\frac{\mathrm{d}N}{\mathrm{d}\,\mathrm{Re}_\theta} = 0.028(H_k - 1) - 0.0345 \exp\left[-\left(\frac{3.87}{H_k - 1} - 2.52\right)^2\right] \tag{63}$$

and

$$\theta \frac{\mathrm{d}\,\mathrm{Re}_\theta}{\mathrm{d}\xi} = -0.05 + \left(\frac{2.7}{H_k - 1}\right) - \left(\frac{5.5}{H_k - 1}\right)^2 + \left(\frac{3}{H_k - 1}\right)^3 + 0.1 \exp\left(\frac{-20}{H_k - 1}\right). \tag{64}$$

The detached flow component $A_{\text{separated}}$ of Eq. (17) is given by Drela [26]

$$\theta A_{\text{separated}} = H_{\text{corr}} \left(0.086 \tanh\left[1.2\left(\log_{10} \mathrm{Re}_\theta - 0.3 + 0.35 \exp\left(-0.15(H_k - 5)\right)\right)\right] - \left(\frac{0.25}{H_k - 1}\right)^{1.5}\right), \tag{65}$$

where the correction term H_{corr} is obtained by

$$H_{\text{corr}} = \begin{cases} 0 & H_{\text{norm}} \le 0, \\ 3H_{\text{norm}}^2 - 2H_{\text{norm}}^3 & 0 < H_{\text{norm}} < 1, \\ 1 & H_{\text{norm}} \ge 1, \end{cases} \tag{66}$$

with

$$H_{\text{norm}} = \frac{H_k - 3.5}{4 - 3.5}. \tag{67}$$

References

[1] Drela, M., and Giles, M. B., "Viscous-Inviscid Analysis of Transonic and Low Reynolds Number Airfoils," *AIAA Journal*, Vol. 25, 1987, pp. 1347–1355. https://doi.org/10.2514/3.9789.

[2] Drela, M., and Giles, M. B., "ISES - A two-dimensional viscous aerodynamic design and analysis code," *25th AIAA Aerospace Sciences Meeting*, 1987, p. 424. https://doi.org/10.2514/6.1987-424.

[3] Aftosmis, M., Berger, M., and Alonso, J., "Applications of a Cartesian mesh boundary-layer approach for complex configurations," *44th AIAA Aerospace Sciences Meeting and Exhibit*, Vol. 11, 2006, p. 652. https://doi.org/10.2514/6.2006-652.

[4] Drela, M., "XFOIL: An Analysis and Design System for Low Reynolds Number Airfoils," *Low Reynolds number aerodynamics*, Vol. 54, Springer, 1989, pp. 1–12. https://doi.org/10.1007/978-3-642-84010-4_1.

[5] Ozdemir, H., van Garrel, A., Koodly Ravishankara, A., Passalacqua, F., and Seubers, H., "Unsteady interacting boundary layer method," *35th Wind Energy Symposium*, 2017, p. 2003. https://doi.org/10.2514/6.2017-2003.

[6] Ye, B., "The Modeling of Laminar-to-turbulent Transition for Unsteady Integral Boundary Layer Equations with High-order Discontinuous Galerkin Method," Ph.D. thesis, Delft University of technology, 2015. URL http://resolver.tudelft.nl/uuid:9f8fb128-b80a-4850-b12c-3a11a5137c99.

[7] Nishida, B., and Drela, M., "Fully simultaneous coupling for three-dimensional viscous/inviscid flows," *13th Applied Aerodynamics Conference*, 1995, p. 1806. https://doi.org/10.2514/6.1995-1806.

[8] Kinney, D., Hafez, M., and Gelhausen, P., "An unstructured full potential-integral boundary layer formulation," *15th Applied Aerodynamics Conference*, 1997, p. 2258. https://doi.org/10.2514/6.1997-2258.

[9] Giles, M. B., and Drela, M., "Two-dimensional transonic aerodynamic design method," *AIAA journal*, Vol. 25, No. 9, 1987, pp. 1199–1206. https://doi.org/10.2514/3.9768.

[10] Van Es, B., "Comparison and Application of Unsteady Integral Boundary Layer Methods using various numerical schemes," Ph.D. thesis, Delft University of technology, 2009. URL http://resolver.tudelft.nl/uuid:5b8b9a14-0ba7-42ec-b7e9-0c4d1608dded.

[11] Bijleveld, H., and Veldman, A., "Prediction of unsteady flow over airfoils using a quasi-simultaneous interaction method," *Wind Energy*, 2013.

[12] Goldstein, S., "On laminar boundary-layer flow near a position of separation," *The Quarterly Journal of Mechanics and Applied Mathematics*, Vol. 1, No. 1, 1948, pp. 43–69. https://doi.org/10.1093/qjmam/1.1.43.

[13] van Dommelen, L. L., and Shen, S.-F., "The spontaneous generation of the singularity in a separating laminar boundary layer," *Journal of Computational Physics*, Vol. 38, No. 2, 1980, pp. 125–140. https://doi.org/10.1016/0021-9991(80)90049-2.

[14] Leballeur, J., "Computation of viscous flows over airfoils, including separation, with a coupling approach," *Computation of Viscous-Inviscid Interaction Symp.*, 1983, p. 1.

[15] Whitfield, D. L., "Integral solution of compressible turbulent boundary layers using improved velocity profiles," *Final Report*, 1978.

[16] Lock, R., and Williams, B., "Viscous-inviscid interactions in external aerodynamics," *Progress in Aerospace Sciences*, Vol. 24, No. 2, 1987, pp. 51–171. https://doi.org/10.1016/0376-0421(87)90003-0.

[17] Veldman, A., "A calculation method for incompressible boundary layers with strong viscous-inviscid interaction," *Proceedings of the Third GAMM—Conference on Numerical Methods in Fluid Mechanics: DFVLR, Cologne, October 10 to 12, 1979*, Springer, 1979, pp. 285–294. https://doi.org/https://link.springer.com/chapter/10.1007/978-3-322-86146-7_29.

[18] Veldman, A. E. P., "New, quasi-simultaneous method to calculate interacting boundary layers," *AIAA journal*, Vol. 19, No. 1, 1981, pp. 79–85. https://doi.org/https://doi.org/10.2514/3.7748.

[19] Veldman, A., Lindhout, J., De Boer, E., and Somers, M., "Vistrafs: a simulation method for strongly interacting viscous transonic flow," *Numerical and physical aspects of aerodynamic flows IV*, Springer, 1990, pp. 37–51. https://doi.org/https://doi.org/10.1007/978-3-662-02643-4_3.

[20] Veldman, A. E., "A simple interaction law for viscous–inviscid interaction," *Journal of Engineering Mathematics*, Vol. 65, No. 4, 2009, pp. 367–383. https://doi.org/10.1007/s10665-009-9320-0.

[21] Crovato, A., Boman, R., Güner, H., Dimitriadis, G., Terrapon, V., Almeida, H., Prado, A., Breviglieri, C., Cabral, P., and Silva, G., "A full potential static aeroelastic solver for preliminary aircraft design," *18th International Forum on Aeroelasticity and Structural Dynamics*, International Forum on Aeroelasticity and Structural Dynamics, 2019, p. 1. URL https://hdl.handle.net/2268/237955.

[22] Smith, A. M. O., *Transition, pressure gradient and stability theory*, Douglas Aircraft Company, El Segundo Division, 1956.

[23] Van Ingen, J., "A suggested semi-empirical method for the calculation of the boundary layer transition region," *Technische Hogeschool Delft, Vliegtuigbouwkunde, Rapport VTH-74*, 1956.

[24] Crovato, A., "Steady Transonic Aerodynamic and Aeroelastic Modeling for Preliminary Aircraft Design," Ph.D. thesis, Université de Liège, 2020. URL https://orbi.uliege.be/handle/2268/251906.

[25] Crovato, A., Prado, A. P., Cabral, P. H., Boman, R., Terrapon, V. E., and Dimitriadis, G., "A discrete adjoint full potential formulation for fast aerostructural optimization in preliminary aircraft design," *Aerospace Science and Technology*, Vol. 138, 2023, p. 108332. https://doi.org/10.1016/j.ast.2023.108332.

[26] Drela, M., "Two-dimensional transonic aerodynamic design and analysis using the Euler equation," Ph.D. thesis, Massachusetts Institute of Technology, 1986. URL https://dspace.mit.edu/handle/1721.1/14974.

[27] Cebeci, T., and Cousteix, J., *Modeling and Computation of Boundary-Layer Flows*, Springer, 2005. https://doi.org/10.1007/3-540-27624-6.

[28] Wigton, L., and Holt, M., "Viscous-inviscid interaction in transonic flow," *5th Computational Fluid Dynamics Conference*, 1981, p. 1003. https://doi.org/10.2514/6.1981-1003.

[29] White, F., *Viscous Fluid Flow*, Vol. 3, McGraw-Hill Education, 2005. URL https://www.mheducation.com/highered/product/viscous-fluid-flow-white.html.

[30] Goldberg, P., "Upstream history and apparent stress in turbulent boundary layers," Tech. rep., Cambridge, Mass.: Massachusetts Institute of Technology, Gas Turbine Laboratory, 1966. URL http://hdl.handle.net/1721.1/104680.

[31] Bradshaw, P., Ferriss, D., and Atwell, N., "Calculation of boundary-layer development using the turbulent energy equation," *Journal of Fluid Mechanics*, Vol. 28, No. 3, 1967, pp. 593–616. https://doi.org/10.1017/S0022112067002319.

[32] Green, J., and Brooman, J., "Prediction of turbulent boundary layers and wakes in compressible flow by a Lag-Entrainment method," *NASA STI/Recon Technical Report N*, Vol. 77, 1977, p. 29460.

[33] Marusic, I., and Kunkel, G., "Streamwise turbulence intensity formulation for flat-plate boundary layers," *Physics of Fluids*, Vol. 15, 2003, p. 2461. https://doi.org/10.1063/1.1589014.

[34] van Ingen, J., "The eN Method for Transition Prediction. Historical Review of Work at TU Delft," *Proceedings of the 38th AIAA Fluid Dynamics Conference and Exhibit, Seattle, Washington*, 2008. https://doi.org/10.2514/6.2008-3830.

[35] Drela, M., "Integral boundary layer formulation for blunt trailing edges," *7th Applied Aerodynamics Conference*, 1989, p. 2166. https://doi.org/10.2514/6.1989-2166.

[36] Coenen, E., "Viscous-inviscid interaction with the quasi-simultaneous method for 2D and 3D airfoil flow," Ph.D. thesis, PhD thesis, Groningen, 2001.

[37] Schlichting, H., and Gersten, K., *Boundary-layer theory*, springer, 2016. https://doi.org/10.1007/978-3-662-52919-5.

[38] Moran, J., *An introduction to theoretical and computational aerodynamics*, Courier Corporation, 2003.

[39] Hirsch, C., *Numerical Computation of Internal and External Flows: The Fundamentals of Computational Fluid Dynamics*, Elsevier, 2007. https://doi.org/10.1016/B978-0-7506-6594-0.X5037-1.

[40] Kelley, C. T., and Keyes, D. E., "Convergence Analysis of Pseudo-Transient Continuation," *SIAM Journal on Numerical Analysis*, Vol. 35, No. 2, 1998, pp. 508–523. https://doi.org/10.1137/S0036142996304796.

[41] Mulder, W. A., and Van Leer, B., "Experiments with implicit upwind methods for the Euler equations," *Journal of Computational Physics*, Vol. 59, No. 2, 1985, pp. 232–246. https://doi.org/10.1016/0021-9991(85)90144-5.

[42] Geuzaine, C., and Remacle, J.-F., "Gmsh: A 3-D finite element mesh generator with built-in pre-and post-processing facilities," *International journal for numerical methods in engineering*, Vol. 79, No. 11, 2009, pp. 1309–1331. https://doi.org/10.1002/nme.2579.

[43] Von Karman, T., and Tsien, H., "Boundary layer in compressible fluids," *Journal of the Aeronautical Sciences*, Vol. 5, No. 6, 1938, pp. 227–232. https://doi.org/10.2514/8.591.

[44] Gregory, N., and O'reilly, C., "Low-speed aerodynamic characteristics of NACA 0012 aerofoil section, including the effects of upper-surface roughness simulating hoar frost," *Reports and Memoranda No. 3726*, 1970.

[45] Squire, H., and Young, A., "The calculation of the profile drag of aerofoils," Tech. rep., HM Stationery Office, 1937.

[46] Abbott, I. H., and Von Doenhoff, A. E., *Theory of wing sections: including a summary of airfoil data*, Courier Corporation, 2012.

[47] McDevitt, J. B., and Okuno, A. F., "Static and dynamic pressure measurements on a NACA 0012 airfoil in the Ames high Reynolds number facility," Tech. rep., NASA Ames Research Center, 1985. URL https://ntrs.nasa.gov/citations/19850019511.

[48] Balakumar, P., Iyer, P. S., and Malik, M. R., "Turbulence Simulations of Transonic Flows over an NACA-0012 Airfoil," *AIAA SCITECH 2023 Forum*, 2023, p. 0254. https://doi.org/10.2514/6.2023-0254.

[49] Cook, P., McDonald, M., and Firmin, M., "Aerofoil rae 2822-pressure distributions, and boundary layer and wake measurements. experimental data base for computer program assessment," *Experimental Data Base for Computer Program Assessment, AGARD Report AR*, Vol. 138, 1979, p. 47.

[50] Palacios, F., Colonno, M., Aranake, A., Campos, A., Copeland, S., Economon, T., Lonkar, A., Lukaczyk, T., Taylor, T., and Alonso, J., "Stanford University Unstructured (SU^2): An open-source integrated computational environment for multi-physics simulation and design," *51st AIAA Aerospace Sciences Meeting including the New Horizons Forum and Aerospace Exposition*, 2013, p. 287. https://doi.org/10.2514/6.2013-287.

[51] Palacios, F., Economon, T., Aranake, A., Copeland, S., Lonkar, A., Lukaczyk, T., Manosalvas-Kjono, D., Naik, K., Padrón, A., Tracey, B., Variyar, A., and Alonso, J., "Stanford university unstructured (SU^2): Analysis and design technology for turbulent flows," *52nd Aerospace Sciences Meeting*, 2014, p. 243. https://doi.org/10.2514/6.2014-0243.

[52] Witteveen, J., Doostan, A., Pecnik, R., and Iaccarino, G., "Uncertainty quantification of the transonic flow around the RAE 2822 airfoil," *Center for Turbulence Research, Annual Briefs, Stanford University*, 2009.

[53] Wang, Z., Fidkowski, K., Abgrall, R., Bassi, F., Caraeni, D., Cary, A., Deconinck, H., Hartmann, R., Hillewaert, K., Huynh, H., Kroll, N., May, G., Persson, P.-O., van Leer, B., and Visbal, M., "High-order CFD methods: current status and perspective," *International Journal for Numerical Methods in Fluids*, Vol. 72, No. 8, 2013, pp. 811–845. https://doi.org/10.1002/fld.3767.

[54] Slater, J. W., Dudek, J. C., and Tatum, K. E., "The NPARC alliance verification and validation archive," *2000 Fluids Engineering Summer Conference*, 2000, pp. –.

[55] Rudnik, R., "Untersuchung der leistungsfähigkeit von zweigleichungs-turbulenzmodellen bei profilumströmungen," Ph.D. thesis, 1997.

[56] Economon, T. D., Palacios, F., Copeland, S. R., Lukaczyk, T. W., and Alonso, J. J., "SU2: An open-source suite for multiphysics simulation and design," *Aiaa Journal*, Vol. 54, No. 3, 2016, pp. 828–846. https://doi.org/10.2514/1.J053813.

[57] Allmaras, S. R., and Johnson, F. T., "Modifications and clarifications for the implementation of the Spalart-Allmaras turbulence model," *Seventh international conference on computational fluid dynamics (ICCFD7)*, Vol. 1902, ICCFD7-1902 Big Island, Hawaii, 2012, pp. 1–11.

[58] Dechamps, P., Crovato, A., Dimitriadis, G., and Terrapon, V. E., "Three-dimensional pseudo-unsteady viscous-inviscid interaction for wings in transonic flow," *AIAA SCITECH 2024 Forum*, 2024, p. 1947. https://doi.org/10.2514/6.2024-1947.

[59] Falkneb, V., and Skan, S. W., "Solutions of the boundary-layer equations," *The London, Edinburgh, and Dublin Philosophical Magazine and Journal of Science*, Vol. 12, No. 80, 1931, pp. 865–896. https://doi.org/10.1080/14786443109461870.

[60] Thomas, J., "Integral boundary-layer models for turbulent separated flows," *17th Fluid Dynamics, Plasma Dynamics, and Lasers Conference*, 1984, p. 1615. https://doi.org/10.2514/6.1984-1615.

[61] LeBalleur, J., "Strong matching method for computing transonic viscous flows including wakes and separations: Lifting airfoils," *La Recherche Aerospatiale, Bull. Bimestriel,(Paris)*, 1981, pp. 161–185.